UNIVERSIDADE TECNOLÓGICA FEDERAL DO PARANÁ
PROGRAMA DE PÓS-GRADUAÇÃO EM ENGENHARIA ELÉTRICA E INFORMÁTICA INDUSTRIAL

HECTOR LISE DE MOURA

PARAMETER AND SURFACE ESTIMATION IN ULTRASOUND NON-DESTRUCTIVE TESTING

TESE

CURITIBA
2021

HECTOR LISE DE MOURA

PARAMETER AND SURFACE ESTIMATION IN ULTRASOUND NON-DESTRUCTIVE TESTING

Estimação de Parâmetros e Superfícies em Ensaios Não-Destrutivos por Ultrassom

Tese apresentado(a) como requisito parcial à obtenção do título de Doutor(a) em Engenharia Elétrica e Informática Industrial, do Programa de Pós-Graduação em Engenharia Elétrica e Informática Industrial, da Universidade Tecnológica Federal do Paraná.

Orientador(a): Prof(a). Dr(a). Daniel Rodrigues Pipa
Coorientador(a): Prof(a). Dr(a). Giovanni Alfredo Guarneri

CURITIBA

2021

Ministério da Educação
Universidade Tecnológica Federal do Paraná
Câmpus Curitiba

HECTOR LISE DE MOURA

PARAMETER AND SURFACE ESTIMATION IN ULTRASOUND NON-DESTRUCTIVE TESTING

Trabalho de pesquisa de doutorado apresentado como requisito para obtenção do título de Doutor Em Ciências da Universidade Tecnológica Federal do Paraná (UTFPR). Área de concentração: Engenharia De Automação E Sistemas .

Data de aprovação: 29 de Abril de 2021

Prof Daniel Rodrigues Pipa, Doutorado - Universidade Tecnológica Federal do Paraná

Prof Heloi Francisco Gentil Genari, Doutorado - Universidade Federal do Abc

Prof Marco Jose Da Silva, Doutorado - Universidade Tecnológica Federal do Paraná

Prof Ricardo Tokio Higuti, Doutorado - Universidade Estadual Paulista - Unesp

Prof Thiago Alberto Rigo Passarin, Doutorado - Universidade Tecnológica Federal do Paraná

ACKNOWLEDGEMENTS

I am deeply thankful to my advisor, Professor Daniel R. Pipa, for introducing me to the field of research and for many years of guidance and insightful advices.

My co-advisor, Professor Giovanni A. Guarneri, was, as well, a great advisor. His careful notes and incentive to approach each problem calmly and carefully were instrumental to my work.

I am also thankful to my wife, Lana B. Baroni, for all her support and patience during times in which I lacked confidence. Thank you for helping me keep my life balanced and healthy.

My parents, Rene and Stella, and parents-in-law, Waldir and Beatriz, who were always supportive of and interested in my work. It means a lot, thank you.

My colleague and friend, Tatiana A. Prado, who provided not only invaluable help to this work but also her friendship.

I would also like to thank my friends and colleagues for the exchange of ideas and camaraderie.

I would like to express my gratitude to PETROBRAS/CENPES and CNPq, for the financial support through the project 311726/2018-6.

“The most important step a man can take. It’s not the first one, is it? It’s the next one. Always the next step, Dalinar.”

— Brandon Sanderson, Oathbringer

RESUMO

MOURA, Hector. **Estimação de Parâmetros e Superfícies em Ensaios Não-Destrutivos por Ultrassom**. 2021. 82 f. Tese (Doutorado em Engenharia Elétrica e Informática Industrial) – Universidade Tecnológica Federal do Paraná. Curitiba, 2021.

Técnicas com ultrassom possuem um papel importante na área de Ensaios Não-Destrutivos. As vantagens do uso de ultrassom são seu baixo custo, portabilidade e uso seguro. O uso de imageamento por ultrassom facilita a localização e caracterização de defeitos internos, bem como a detecção e mapeamento de áreas corroídas. O processo de imageamento pode ser feito de diferentes maneiras, porém, em todas, parâmetros de inspeção como velocidade de propagação do som em diferentes meios, assim como a interface entre meios, devem ser conhecidos. Premissas incorretas nesses parâmetros levam a distorções nas imagens resultantes. Essas distorções podem prejudicar a detecção e caracterização de defeitos. A estimação desses parâmetros, geralmente, é feita por calibração usando procedimentos e materiais específicos. Os objetivos deste estudo são: (1) desenvolver métodos para estimação de parâmetros durante a inspeção e sem a necessidade de materiais específicos, assim como (2) reconstrução de superfícies para mapear a corrosão em tubulações. Para o primeiro objetivo, é mostrado que algoritmos de imageamento comuns, como o *Total Focusing Method*, podem ser usados para estimar a velocidade de propagação do som nos material imageado. O método proposto consegue realizar uma estimativa sem a necessidade de uma busca em grade, atingindo uma redução de iterações de 8000 para até 23, com a mesma tolerância quando comparado a métodos presentes na literatura. Para o segundo objetivo, foi proposto um método para estimar o perfil 1D de superfícies. Esse método inédito é formulado como um problema inverso. Esse problema é definido como uma soma de mínimos quadrados ponderados com regularização *Total Variation* de segunda ordem, dessa forma, favorecendo soluções lineares por partes. O método desenvolvido se mostrou mais robusto a ruído do que outros métodos da literatura. Em comparação com o método estado da arte, o método proposto obteve erros menores em até uma ordem de grandeza. Quando os perfis estimados foram usados para o imageamento do interior de objetos, o método proposto também forneceu imagens melhores que possibilitam melhor detecção dos defeitos presentes.

Palavras-chave: Processamento Digital de Sinais. Ensaios Não-Destrutivos. Estimação de Parâmetros.

ABSTRACT

MOURA, Hector. **Parameter and Surface Estimation in Ultrasound Non-Destructive Testing**. 2021. 82 p. Thesis (PhD in Electrical and Computer Engineering) – Universidade Tecnológica Federal do Paraná. Curitiba, 2021.

Ultrasound techniques play an important role in Non-Destructive Testing. The advantages of ultrasound are its low-cost, portability and safety. Ultrasound imaging facilitates the localization and characterization of internal defects, as well as the detection and mapping of corroded areas. The imaging process can be done in different ways, but common to all, inspection parameters such as sound speed in the different media, as well as the interface between these media, must be known. Wrong assumptions on these parameters lead to distortions in the resulting images that could, potentially, hinder the characterization of defects. Estimation of these parameters is usually done by calibration using specific materials and procedures. The objectives of this study are to develop (1) methods to estimate such parameters during inspection time, without the need for specific materials, as well as (2) surface reconstruction methods to address corrosion mapping in pipes. In the first objective, it is shown that commonly used imaging processes, such as the Total Focusing Method, can be used to estimate the sound speed in the imaged material with low uncertainty. The proposed method does a gridless search in a given interval and is able to produce an estimate in up to 23 iterations, from the 8000 iterations needed, for the same tolerance, in the methods present in the literature. In the second objective, a method for estimating a 1D surface profile is proposed. This new method weights the contribution of each surface point as a way to cope with different SNR levels. Also, by means of a second-order Total Variation regularization, the method promotes piecewise linearity in the solution while suppressing noise. The developed method is shown to be more robust in the presence of noise than other methods in the literature. When compared to the state-of-the-art, the proposed method obtained errors almost ten-fold smaller. Using the estimated profiles to produce interior images of the objects, the proposed method lead to more accurate images, enabling better detection of the flaws.

Keywords: Digital Signal Processing. Non-Destructive Testing. Parameter Estimation.

LIST OF ALGORITHMS

LIST OF FIGURES

LIST OF TABLES

LIST OF ACRONYMS

INITIALISM

ADMM	Alternating Direction Method of Multipliers
AWGN	Additive White Gaussian Noise
CPWC	Coherent Plane Wave Compounding
DWI	Divergent Wave Imaging
fADMM	fast ADMM
FMC	Full Matrix Capture
GSS	Golden Section Search
IQA	Image Quality Assessment
MSE	Mean Squared Error
NDE	Non-Destructive Evaluation
NDT	Non-Destructive Testing
PWI	Plane Wave Imaging
SDH	Side-Drilled Hole
SNR	Signal-to-Noise Ratio
TFM	Total Focusing Method
TV	Total Variation
UA	Ultrassound Array
WLS	Weighted Least Squares

ACRONYMS

EMAT	ElectroMagnetic Acoustic Transducer
LIFU	Laser-Induced Focused Ultrasound
ROI	Region of Interest
SAFT	Synthetic Aperture Focusing Technique

CONTENTS

1 INTRODUCTION

In the oil industry, specially in offshore platforms, the safe operation of pipelines is crucial. As stopping production and replacing sections of a pipeline is a very costly process, regular inspections of structural health are needed. If, during an inspection, it is detected that the damage to the pipeline has exceeded a given threshold, then the damaged section must be replaced. This helps to reduce the costs by stopping production only when it is strictly necessary. Figure 1 shows an example of a corroded half pipe, this sample was removed from operation after an inspection. For submarine inspections, ultrasound techniques can be used for damage assessment.

Figure 1 – A Corroded half pipe that was removed of operation for analysis.

Source: Own.

In Non-Destructive Evaluation (NDE), also known as Non-Destructive Testing (NDT), ultrasound techniques are widely used for detecting and sizing defects such as voids, cracks and others, as well as for measuring the remaining thickness of corroded specimens. Ultrasound array systems for ultrasonic imaging have become standard in industrial NDE due to their capabilities of beam focusing, steering and electronic scanning. Images of a cross-sectional view are called a B-scan, for Brightness scan, which is one of the most common kind of images generated with ultrasound.

To evaluate the reflectivity, or brightness, throughout the Region of Interest (ROI), conventional phased-array relies on delay laws applied at transmission and reception. These delay laws allow the focusing of waves at specific points. Then, an image can be formed, or

reconstructed, by repeating this procedure for every point of a discretized ROI. Depending on the number of points in the ROI, this process may be prohibitively time-consuming.

One way of reducing the reconstruction time is to emit several unfocused waves and post-process the received data using imaging algorithms such as the Synthetic Aperture Focusing Technique (SAFT) (DOCTOR *et al.*, 1986; STEPINSKI, 2007), the Total Focusing Method (TFM) (HOLMES *et al.*, 2005; HUNTER *et al.*, 2008) and Coherent Plane Wave Compounding (CPWC) (MONTALDO *et al.*, 2009). These techniques depend on prior knowledge such as the wave propagation speed in the specimen and, in the case of immersion testing, the wave propagation speed in the coupling medium and the surface geometry of the inspected object.

In the case of a mismatch between the assumed and actual speeds, the recovered image will be distorted, making it harder to correctly determine the location and characteristics of flaws. Similarly, a wrong assumption on the geometry of the interface will result in malformed images.

In this study, methods to estimate inspection parameters, such as sound speed and surface profile of immersed objects, will be analyzed. The use of the surface profile estimation to map corroded interior surfaces is analyzed as well. Experiments are carried out on both simulated and experimental data to ensure practicality.

This document is organized as follows: Chapter 2 reviews the literature of NDE to establish its basic notions; Chapter 3 describes the sound speed estimation method; Chapter 4 describes the 1D surface profile estimation method developed; finally, Chapter 5 summarizes the results obtained and details the next steps in the development of both methods.

1.1 GENERAL OBJECTIVE

The objective of this research is to develop methods of estimating inspection parameters from acquired data. These methods must work in real-world scenarios without the need for reference specimens.

1.2 SPECIFIC OBJECTIVES

1. To reproduce the state-of-the-art method, and results, presented in (TREEBY *et al.*, 2011) in order to establish a baseline for comparison on sound speed estimation.

2. To reproduce the state-of-the-art method, and results, presented in (MALKIN *et al.*, 2018) in order to establish a baseline for comparison on surface profile estimation.

3. To improve on the search method used in (TREEBY *et al.*, 2011) in order to reduce the number of iterations required to reach the same tolerance level.

4. To create a method for surface profile estimation based on second-order Total-Variation regularized inverse problems.

5. To choose a suitable algorithm for solving the proposed formulation within the time limitations of the imaging process.

1.3 SUBMITTED PAPERS

The method for sound speed estimation presented in this study is based on the one described in (MOURA *et al.*, 2020). This thesis contains excerpts and extensions of the following articles.

1. H. L. Moura *et al.*, (2019) “Image-based ultrasound speed estimation for NDT in homogeneous media”, Review of Progress in Quantitative Nondestructive Evaluation.

2. H. L. Moura *et al.*, (2020) “Image-Based Ultrasound Speed Estimation in Isotropic Materials”, in IEEE Sensors Journal, doi: 10.1109/JSEN.2020.3002853.

3. H. L. Moura *et al.*, (under review) “Surface Estimation via Analysis Method: A Constrained Inverse Problem Approach”, submitted to IEEE Transactions on Ultrasonics, Ferroelectrics, and Frequency Control.

2 ULTRASOUND NDE

This chapter reviews the available literature in order to establish the basic notions of NDE. The understanding of these notions is necessary since the proposed methods build upon these notions.

2.1 ULTRASOUND TESTING

NDE can be simply defined as an examination performed on an object in order to evaluate the material characteristics and presence of flaws, for example, in a way that do not alter the object (HELLIER, 2020, Chapter 1). NDE is present in every major industry, if not all, and plays a major role in preventing failures. It can be applied in different stages of a product life-cycle, during production (RIEDER *et al.*, 2014; EVERTON *et al.*, 2016; MILLON *et al.*, 2018) and after deployment to ensure its safe operation (MAIERHOFER, 2003; LE *et al.*, 2017; GIURGIUTIU; CUC, 2005). The monitoring of a structure, or product, is done in order to prevent failure during service. For example, aircrafts often undergo inspection to ensure it is safe for flight (HSU, 2013). Bridges (LEE *et al.*, 2014; LE *et al.*, 2017) and pipelines (CARVALHO *et al.*, 2008; RIZZO *et al.*, 2010) also undergo regular inspections to monitor their integrity.

Technologies applied to NDE include, but are not limited to: visual testing, radiographic testing, ultrasonic testing, eddy current testing and thermal infrared testing. The development of ultrasound equipment for NDE dates back to the first half of the 20^{th} century (HELLIER, 2020). Even so, most articles about it date back to the 1970s (ADLER; LEWIS, 1976; KINO, 1979; BORLOO, 1973; KRAUT, 1976). It presents a quick, safe and cost-effective method for in-situ detection of flaws in manufactured parts. It is applied in a wide range of industry applications, from nuclear energy to aircraft inspection (KINO, 1979).

Figure 2 illustrates an ultrasound inspection using a monolithic probe i.e. a single element probe. In this scenario, the probe is placed in three different positions. At each position, the transducer is fired and the echoes are recorded. The recorded signal is called an Amplitude-scan, or A-scan. A flaw in the object will generate an echo with amplitude dependent on the flaw size. Also, the angle relative to the normal of the probe affects the amplitude of the echo.

By moving the probe and performing acquisitions at each position, the recorded A-scans can be used to form a cross-section image of the object, termed B-scan. Figure 3 illustrates

Figure 2 – Example of ultrasound inspection. An ultrasonic probe placed in three different positions over an object and the respective A-scans obtained in each position. The red dashed lines indicate the beam spread. Note that flaws near the limit of beam spread give a lower amplitude echo compared to a flaw placed right under the probe.

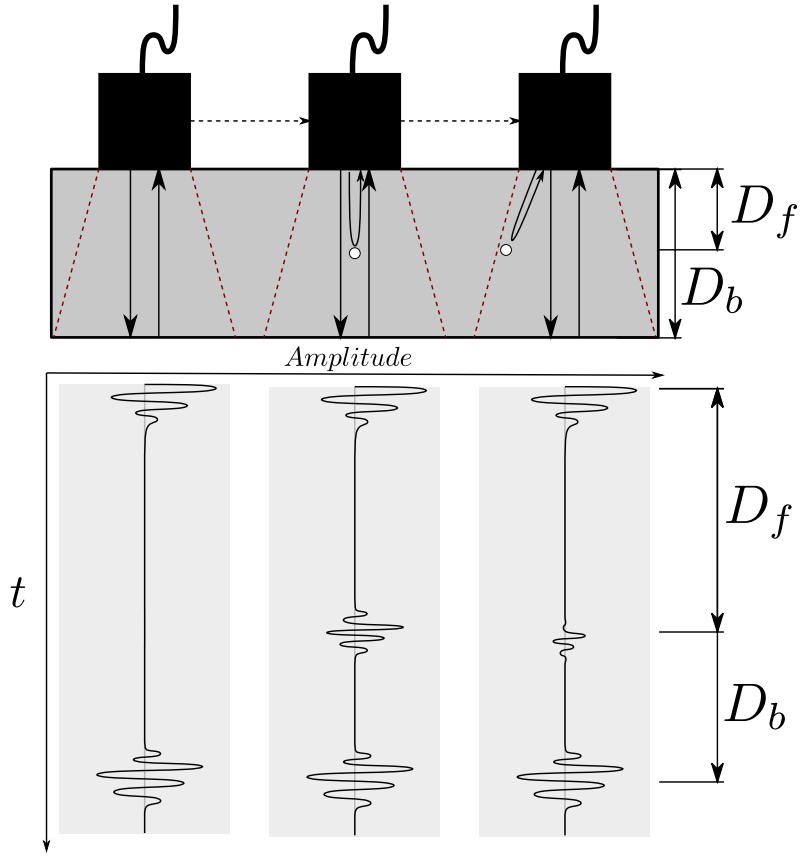

Source: Own.

a B-scan of one of the flaws in Figure 2. The grouping of A-scans side-by-side is one simple way of obtaining a B-scan. This kind of B-scans presents poor lateral resolution but, as will be explained in Section 2.3, the use of more advanced techniques can greatly improves that.

In some situations, it is convenient to transmit waves with an incident angle different from zero. In such cases, a wedge can be used to couple the probe to the object in a way that the waves enter the object at the desired angle, as shown in Figure 4. Wedges can also be used for coupling the probe to different geometries, and in this case a wedge must either be specifically designed for the target geometry or be conformable (LONG; CAWLEY, 2008).

Different transducer technologies were developed that can overcome some of the restrictions of wedges, such as Ultrassound Array (UA), ElectroMagnetic Acoustic Transducer (EMAT), and Laser-Induced Focused Ultrasound (LIFU) (DIXON *et al.*, 1999; HWANG *et al.*, 2000; SONG *et al.*, 2002; DIXON *et al.*, 2011). These technologies enabled more flexible and informative inspections. An example of that is the possibility of focusing, and steering, beams

Figure 3 – (a) A simple B-scan can be formed by placing A-scans side-by-side to form an image. (b) A water-fall plot of the A-scans placed side-by-side.

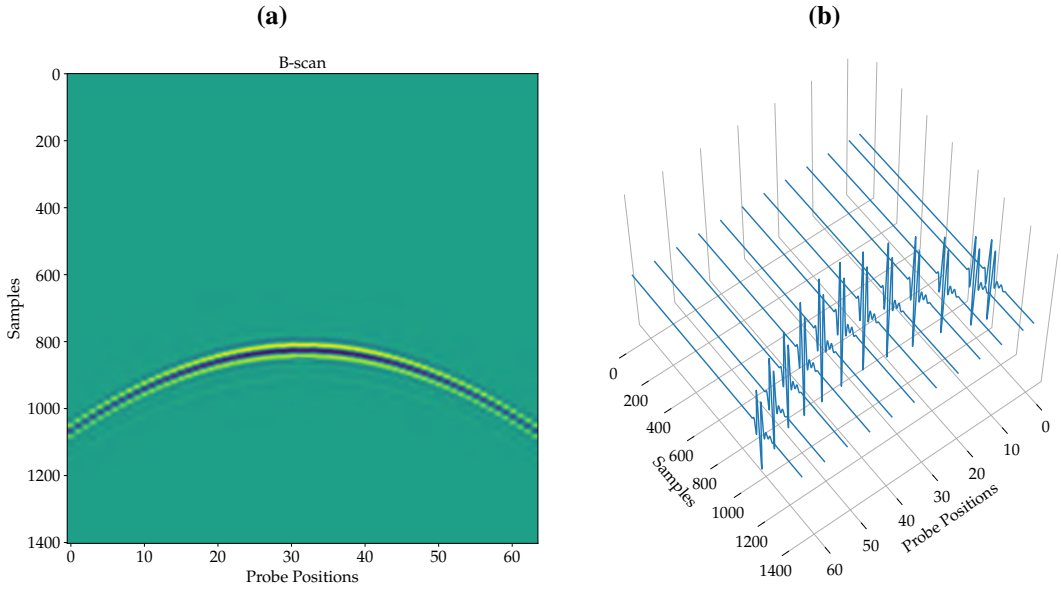

Source: Own.

Figure 4 – An wedge can be used to transmit waves at different angles in order to reach certain points of the object.

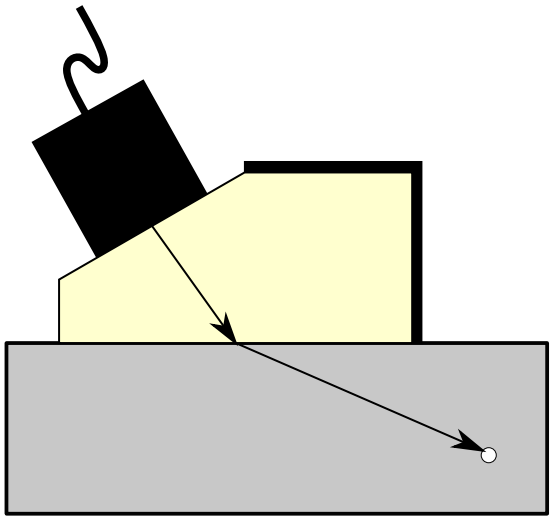

Source: Own.

with UAs. The use of UAs has become an industrial standard (TREMBLAY *et al.*, 2013) and will be the focus of this review.

2.2 ULTRASOUND ARRAYS

UAs are made of small piezoelectric transducer elements in a single casing. These elements are wired independently, so that elements can be driven separately and the echo signals can be received in parallel (SCHMERR, 2014, Chapter 1).

UAs can also have multiple element geometries and distributions. The most common configurations are the linear arrays and the matrix arrays. Linear arrays are composed of several rectangular elements arranged side-by-side in the x-axis. The elements dimensions are much smaller on the x-axis than on the y-axis, as shown in Figure 5(a). Due to the smaller length on the x-axis, the waves generated by the elements are more divergent than in the y-axis (SCHMERR, 2014, Chapter 4). This divergence is what enables the steering and focus of the wavefront. The x-axis is also called the *active direction*. In the y-axis, or the *passive direction*, the wave generated by a single element is closer to a plane-wave due to the length of the element in this direction.

Matrix, or 2-D, arrays are composed of small elements distributed on a plane. These elements can be of any geometry, although squares are more cost-effective (SCHMERR, 2014, Chapter 1). The distribution can be on an uniform grid, as illustrated in Figure 5(b), but is not restricted to it. Some papers (DIARRA *et al.*, 2012; DIARRA *et al.*, 2013; HARPUT *et al.*, 2020) suggest that sparsely distributed elements, with random positions and orientations are capable of generating images with Signal-to-Noise Ratio (SNR) close to those generated by arrays with more elements. Matrix arrays are capable of focusing in volumes, instead of a single plane, and thus allow for volumetric (3D) imaging without movement of the probe.

The emitted wavefront can be manipulated by applying different delays to each element, forming the delay laws. This enables the emitted beam to be steered and/or focused. Different delay laws can be applied in transmission and reception. The process of manipulating the wavefront is called beamforming (SIMONETTI; HUANG, 2008).

Similar to delays, it is also possible to apply individual amplitude gains to each element. These gains are called apodization laws. Apodization is used to tailor the acoustic radiation characteristics of a UA. It is mainly used for reducing the effects of grating lobes in imaging processes. These capabilities are illustrated in Figure 6.

Figure 5 – A linear array (a) with rectangular elements, typically used for 2D imaging. A matrix array (b) with square elements distributed in an uniform grid. Such array can be used for 3D imaging without movement of the probe.

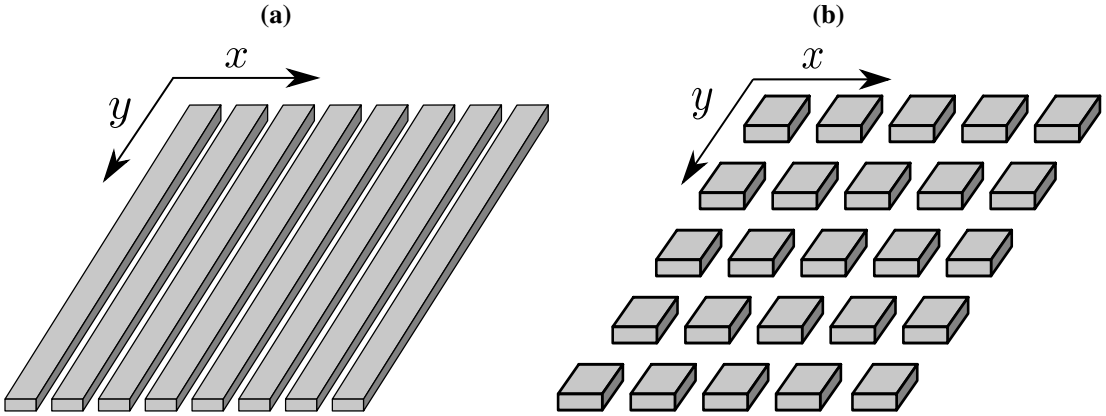

Source: Own.

Figure 6 – (a) Components of an ultrasonic phased array. Different gains and delays can be applied to each element separately to manipulate the emitted beam. In (b), the elements are fired according to a linear delay law to steer the beam. In (c), a non-linear delay law is applied to focus the beam in a given location. These delay laws can also apply steering and focusing to the same beam in order to focus in different directions.

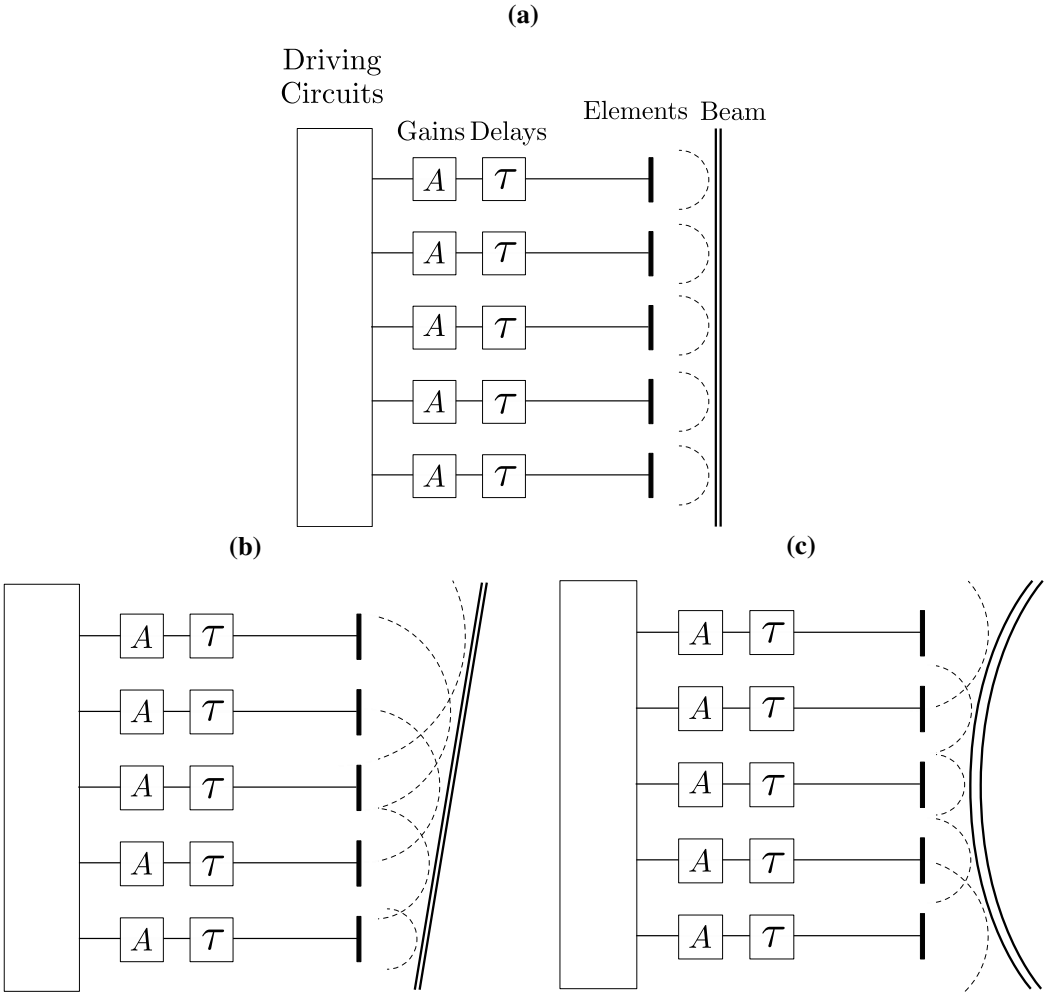

Source: Adapted from Schmerr (2014)

The flexibility in defining different delay laws enables the use of a single UA in different inspection scenarios. For example, a set of delay laws can be used to replace different kinds of wedges, reducing costs and inspection times.

The process of beamforming can also be done in post-processing, that is, after the acquisition is done. In this way, acquisition times can be further reduced if the inspector does not need to see images in real time.

2.3 POST-PROCESSING BEAMFORMING

For post-processing beamforming, several unfocused waves are fired and the echoes are received, in parallel, by other elements in the array. This, sometimes, is called Divergent Wave Imaging (DWI) or Plane Wave Imaging (PWI)(MONTALDO *et al.*, 2009).

One such method of DWI, denoted Full Matrix Capture (FMC), consists in firing each element sequentially while receiving with all other elements. The firing of every element may be time consuming (HOLMES *et al.*, 2004). Figure 7 illustrates the structure of an FMC of a 4-elements probe.

Figure 7 – An FMC of a 4-elements probe. The A-scans, $h_{i,j}[t]$, of every combination of two elements is placed in the matrix. The subscripts i and j denote, respectively, the transmitting and receiving elements.

$$\begin{bmatrix} h_{0,0}[t] & h_{0,1}[t] & h_{0,2}[t] & h_{0,3}[t] \\ h_{1,0}[t] & h_{1,1}[t] & h_{1,2}[t] & h_{1,3}[t] \\ h_{2,0}[t] & h_{2,1}[t] & h_{2,2}[t] & h_{2,3}[t] \\ h_{3,0}[t] & h_{3,1}[t] & h_{3,2}[t] & h_{3,3}[t] \end{bmatrix}$$

Source: Own authorship.

To reconstruct the images from unfocused waves, delays are applied to each A-scan and summed coherently in order to form an image. The main advantage of post-processing beamforming compared to hardware beamforming is the superior flexibility to form the image (TREMBLAY *et al.*, 2013).

In hardware beamforming, one needs to determine which points are going to be focused prior to acquisition. In order to change imaging parameters, a new acquisition must be done. For post-processing beamforming, assuming the A-scans acquired are long enough, different regions can be imaged with only one acquisition set.

Among the ultrasound imaging techniques used in NDE, the most used are SAFT, TFM and CPWC. These techniques are very similar, differing in terms of excitation pattern and amount of data processed. SAFT was originally developed to handle a single-element transducer acquiring signals in different positions. This is equivalent to using only the pulse-echo data from FMC.

TFM uses all data in the FMC (pulse-echo and pitch-catch) and, therefore, presents better SNR in the reconstructed images. The main disadvantage of TFM is that it requires the acquisition of the whole FMC, which can be storage burdensome. There are ways to reduce

storage requirements by undersampling the FMC. For example, by considering the reciprocity theorem (SCHMERR, 2014)[1], a triangular matrix, like the one in Figure 8, can lead to very similar images by using TFM. This undersampled matrix is often called a Half Matrix Capture (HMC) (TREMBLAY *et al.*, 2013).

Figure 8 – An HMC of a 4-elements probe. According to the reciprocity theorem, A-scans $h_{i,j}$ and $h_{j,i}$ are equivalent. In order to make faster acquisitions, it is possible to acquire only one of them and double its amplitude. This is an example of an upper triangular matrix but an HMC could be just as well a lower triangular matrix.

$$\begin{bmatrix} h_{0,0}[t] & 2.h_{0,1}[t] & 2.h_{0,2}[t] & 2.h_{0,3}[t] \\ & h_{1,1}[t] & 2.h_{1,2}[t] & 2.h_{1,3}[t] \\ & & h_{2,2}[t] & 2.h_{2,3}[t] \\ & & & h_{3,3}[t] \end{bmatrix}$$

Source: Own authorship.

When very fast acquisition is required, PWI is the more common approach. This process consists in the emission of several plane-waves steered in different angles. The number of waves emitted can be less than the number of elements in the probe. While the number of waves is reduced, the energy transmitted by each firing is increased.

The CPWC algorithm uses data acquired by PWI. It presents SNR higher than SAFT and, if enough waves are fired in different angles, it presents images very close in SNR to TFM (LE JEUNE, L. *et al.*, 2016a; LE JEUNE, L. *et al.*, 2016b).

2.3.1 Beamforming Methods

For the methods mentioned, the image is formed by a delay and sum process done to time-domain data. The distances between investigated points in the ROI and the piezoelectric elements, as well as the sound speed in the material, are assumed to be known. For SAFT, the 2D image formation in the (x,z)-plane is described as

$$I(x,z) = \left| \sum_{t \in T} A_t(x,z) \cdot h_t\left(\frac{2d_t(x,z)}{c}\right) \right|, \tag{1}$$

where $I(\cdot)$ denotes the reconstructed image, T represents the set of elements in the array, $A_t(\cdot)$ denotes the apodization weights, $h_t(\cdot)$ denotes the analytical signal of the pulse-echo A-scan

[1] The reciprocity theorem states that the A-scan received in element i when a wave is transmitted by element j is equal, ignoring the noise components, to the A-scan received in element j when a wave is transmitted by element i. In other words, the FMC is symmetrical with respect to the transmitting and receiving elements.

Figure 9 – The three presented algorithms are based on applying delays and coherently summing different A-scans. The SAFT algorithm considers only pulse-echo A-scans and the delay depends solely on the distance between the transducer element and the investigated point in the ROI. TFM uses every A-scan possible in the FMC data and the delays are calculated using the distances between emitting and receiving elements to the each point in the ROI. The CPWC algorithm uses the A-scans received by each element when the array fires a plane wave of angle α. The delays are calculated taking into account the distance traveled by the plane wave to the point and the distance from the point to the each receiving element. To evaluate the delays, the total distances are divided by sound speed in the evaluated media.

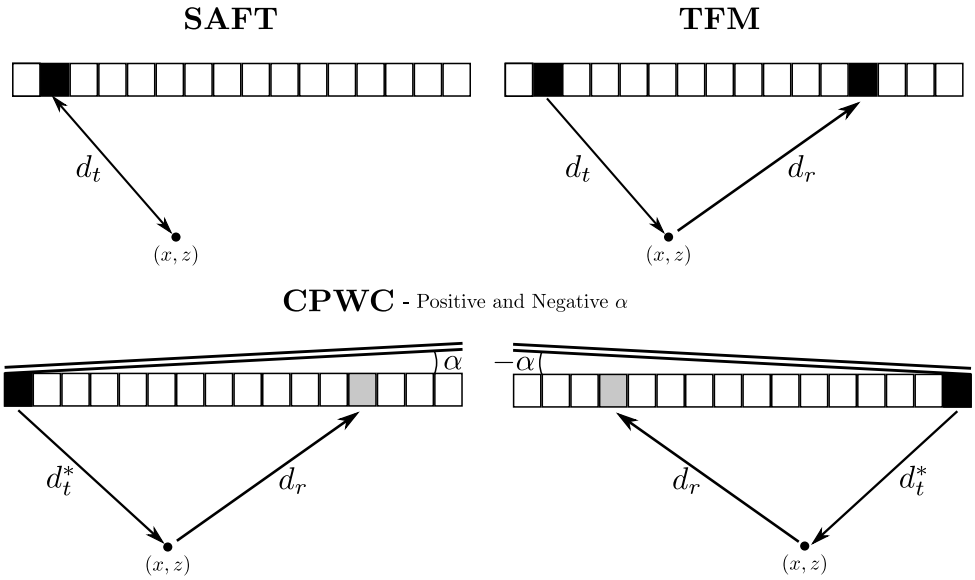

Source: Own authorship.

from element t and $d_t(\cdot)$ denotes the Euclidean distance from the element t to the point (x,z), as shown in Figure 9. For the TFM algorithm, the image is given by

$$I(x,z) = \left| \sum_{t,r \in T} A_{t,r}(x,z) \cdot h_{t,r}\left(\frac{d_t(x,z) + d_r(x,z)}{c} \right) \right|, \tag{2}$$

where $h_{t,r}(\cdot)$ denotes the analytical signal from element obtained when element t is the emitter and element r is the receiver. Similarly, $A_{t,r}(\cdot)$ denotes the apodization weights.

Finally, for CPWC the image formation process is described as

$$I(x,z) = \left| \sum_{\alpha \in \Lambda, r \in T} A_{\alpha,r}(x,z) \cdot h_{\alpha,r}\left(\frac{d_\alpha(x,z) + d_r(x,z)}{c} \right) \right|, \tag{3}$$

where Λ represents a set of emitting angles, $h_{\alpha,r}(\cdot)$ denotes the analytical signal obtained in element r when a plane wave with angle α is emitted and $d_\alpha(\cdot)$ is the distance traveled by the plane wave to the point (x,z), as shown in Figure 9. The distance $d_\alpha(\cdot)$ is defined according to the angle α as

$$d_\alpha = (x - x_e)\sin\alpha + z\cos\alpha, \tag{4}$$

in which x_e denotes the position of the first element to emit. Usually, the apodization weights can be ignored and set to ones. This leads to visual artifacts in the image. One way of deal-

Figure 10 – Images reconstructed with TFM from data acquired in an aluminum block of with an SDH of 1mm radius. The red circles represent the position of the SDH, 40mm below the transducer position. Assuming wrong values of sound speed causes distortion of the SDH echo. The three images were reconstructed assuming different speeds, (a) with assumed 25% lower than actual speed, (b) with actual speed, 6319 m/s, and (c) with assumed speed 25% higher than actual speed.

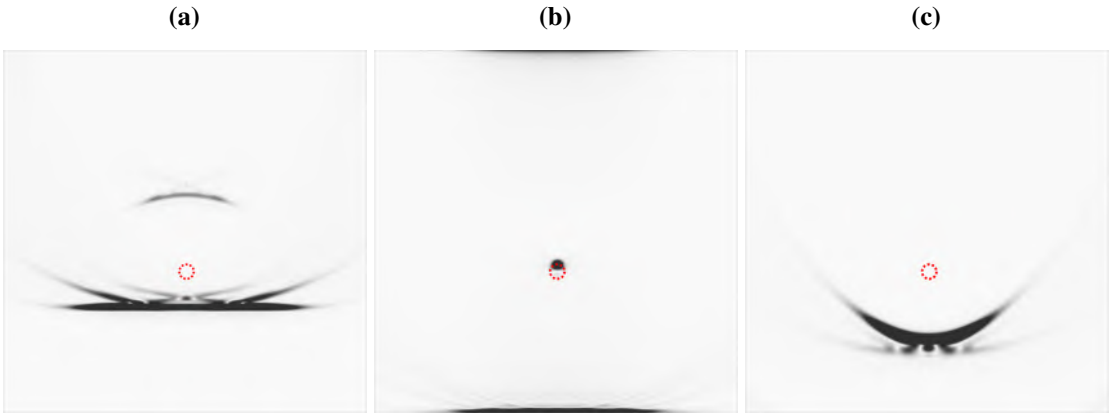

Source: Own authorship.

ing with these is to weight the signals according to the directivity function of the transducer elements (SCHMERR, 2014, Chapter 4).

From Equations (1), (2) and (3) it becomes clear that a mismatch in sound speed affects the imaging process. A mismatch can occur, for example, if the reference speed is measured in different circumstances than those of an inspection. When the assumed sound speed is slightly different from the actual sound speed, the image obtained appears to be blurred. On the other hand, for large mismatches, the image obtained is not homogeneously blurred and follows certain patterns, such as upward and downward curves.

Figure 10 shows three TFM reconstructed images of a Side-Drilled Hole (SDH) in an aluminum block. It illustrates the effect on the reconstructed image when there is a 25%, positive and negative, mismatch in the assumed sound speed in relation to the actual sound speed of 6319 m/s. While a mismatch of 25% will hardly occur in a real scenario, it highlights the effects of a mismatch. In seawater, the sound speed can vary between 1450 m/s and 1570 m/s (DUXBURY, 2020) depending, mostly, on temperature and pressure. This range translates to a mismatch of up to 7.95%. In solids with higher sound speed, mismatches due to differences between reference and calibrated values are expected to be lower. In the case of acrylic, the speed found was 1.5% greater than what is found in a reference table (MATERIAL. . . , 2021).

As the mismatch in sound speed leads to degraded/blurred images, one way to estimate the magnitude of such mismatch is the quantitative evaluation of the degradation present in a

Figure 11 – Example of wave trajectory in an immersion inspection. The trajectories are dependent on the position of the elements, the point investigated and the sound speed in both media.

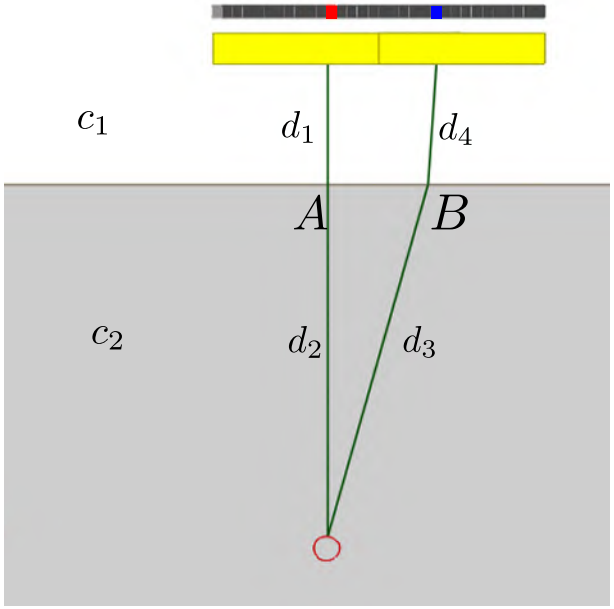

Source: Own authorship.

given reconstructed image. Chapter 3 reviews major concepts of Image Quality Assessment (IQA) that can be used to this end.

2.4 IMAGING THROUGH SURFACES

Figure 11 illustrates a scenario where the inspected object is immersed in fluid for coupling with the probe. This is usually done when the inspected object has an irregular surface and the probe cannot be placed in direct contact with it. In such cases, imaging the interior of the object becomes more complex as the waves are refracted by the surface. The refraction is dependent on the incidence angle and the sound speed in both materials. This relation is given by Snell's Law.

Once the trajectories are calculated, based on estimated sound speeds and objects surface, a TFM image can be formed according to

$$I(x,z) = \left| \sum_{t,r \in T} A_{t,r}(x,z) \cdot h_{t,r} \left(\frac{d_{ta}(x,z) + d_{br}(x,z)}{c_1} + \frac{d_a(x,z) + d_b(x,z)}{c_2} \right) \right|, \tag{5}$$

where $d_{ta}(\cdot)$ and $d_a(\cdot)$ denote the distances from point A in the surface to the transmitting element and to the interior point (x,z), respectively. Similarly, $d_{br}(\cdot)$ and $d_b(\cdot)$ denote the distances from point B in the surface to the receiving element and to the interior point (x,z), respectively.

Figure 12 – Images reconstructed with TFM from simulated data of three SDHs inside a steel cylinder. Image (a) shows the SDHs when the surface is exactly known. Image (b) shows the same region but with a rough estimated surface. Both images are displayed in dB scale.

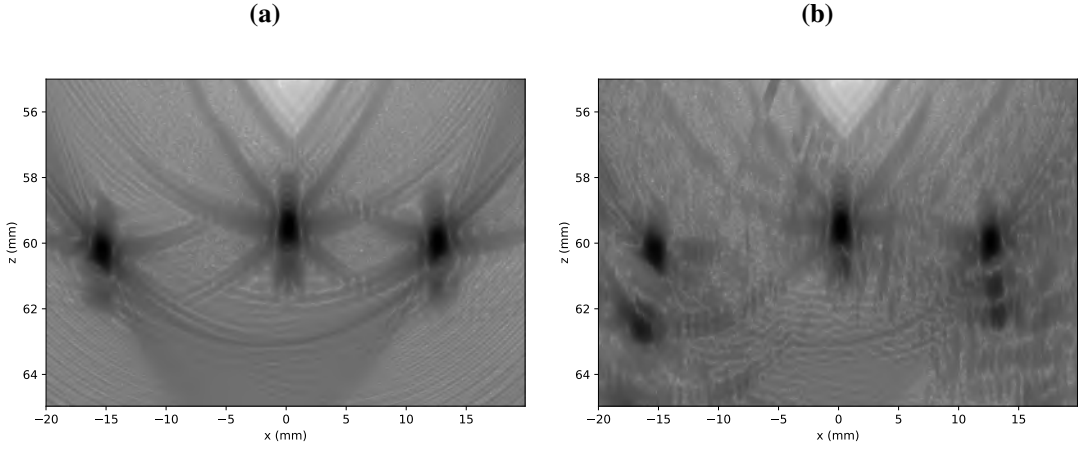

Source: Own authorship.

In the case of a faulty estimated surface, the trajectories calculated will not correspond to the truth. These will, in turn, lead to artifacts and loss of coherence in the reconstructed images. These effects are illustrated in Figure 12. Also, if there is a mismatch in sound speed inside the object, the trajectories will be wrong, causing other artifacts besides the apparent blur. In Chapter 4, methods of estimating the surface of objects will be revised and a new method will be presented in details.

2.5 IMAGE STITCHING

The inspection of large objects require the probe to be moved along a trajectory. At each point of the trajectory, an acquisition is made and, from it, an image can be formed. The images associated with each position can be analyzed individually or combined together in a larger image. The process of combining the images is called image stitching (BROWN; LOWE, 2007).

This process is commonly used for creating panoramic images from different photos with some overlap. By knowing the movement of the camera between different photos, algorithms can make the necessary transformations, such as translation and rotation, to position images together correctly. Brown and Lowe (2007) showed that different images must be blended carefully in order to reduce artifacts. This is illustrated in Figure 13.

Figure 13 – Example of an image stitching method for panoramic photos. In (a) only half of the captured images are present, to better illustrate the individual transformations. (b) shows the photos stitched with no gain correction or blending. (c) shows the same photos combined using gain correction and alpha blending.

(a)

(b)

(c)

Source: Adapted from Brown and Lowe (2007).

The blending between images is usually done via alpha-blending, where an image slowly turns transparent while overlapping with another image. This is similar to to a weighted averaging of pixels, where pixels near the border of their corresponding images have smaller weights. This allows for smooth transitions, making the "seams" between images subtle.

Although similar, image stitching for ultrasound images has important differences, for example, a B-scan image shows a cross-section view of the scene. Another difference is the illumination, which in the case of ultrasound imaging comes from the probe. Depending on the orientation of reflectors in a certain region, the waves reflected may not reach the probe again. Because of this, pixels in an overlapped region can be brighter in one image and dimmer in another.

Figure 14 – Difference between stitching methods. Averaging the overlapping pixels leads to a final image with clear seams and lower contrast. By keeping the maximum valued pixel the transitions are more subtle and the visual quality of the image is increased. Images are in logarithmic scale for better visualization of the differences.

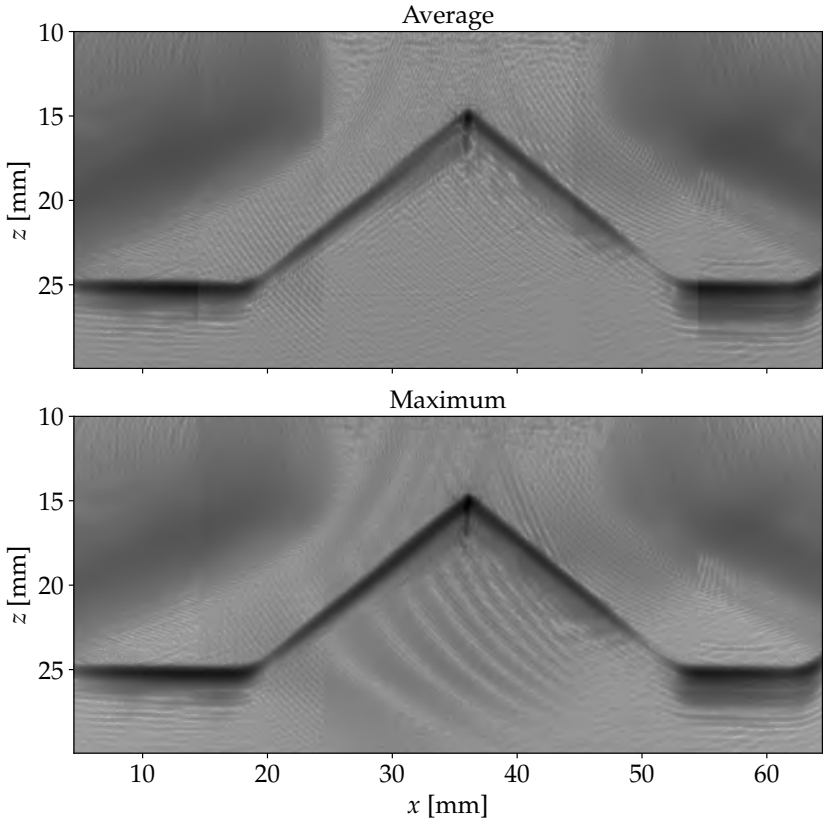

Source: Own authorship.

Malkin *et al.* (2018) proposed to average the pixels in overlapped regions. As stated before, pixels that correspond to the same region, but in different images, can have different values of brightness according to probe positioning. By averaging these pixels, SNR is lost and contrast is diminished. McKee *et al.* (2020) proposed the use of the maximum valued pixels to be used in overlapping regions. The SNR is mantained since there is no loss of signal amplitude or amplification of noise. This also leads to subtle transitions between images, as demonstrated in Figure 14. From here on, the process of image stitching will refer to combining images by keeping the maximum valued pixels in overlapped regions.

2.6 COMMENTARIES

This chapter reviewed the basic notions of NDE, as well as the role of ultrasound in NDE. Also, the advantages of using UAs and post-processing beamforming for inspections. Common methods for post-processing beamforming, SAFT, TFM and CPWC, were introduced

and detailed. Along with the methods, some of the problems associated with wrong inspection parameters were demonstrated. Additionally, the method of combining images of different and overlapping regions, called stitching, was defined.

3 SOUND SPEED ESTIMATION

Generally, sound speed must be calibrated prior to every inspection. This calibration is done using a specimen of the same material as the inspected object, but with known geometry, so that the echoes can be related to a known distance, as illustrated in Figure 15. Frequently, the exact conditions of the inspection cannot be reproduced during calibration, which may lead to errors. In submarine inspections, for instance, parameters such as pressure, salinity and temperature influence the sound speed in water (WONG; ZHU, 1995) and the estimation and reproduction of such conditions beforehand is impractical. To avoid such complications, a reference-free calibration method is desired.

Figure 15 – Scheme for sound speed calibration with specimen of known geometry for both contact and immersion testing. The sound speed in the specimen, c_s, may be estimated from the total distance traveled by the wave inside the specimen, $2D_s$, divided by the round-trip time measured between two backwall echoes, t_{Bw}. In the case of immersion testing, the sound speed in the water, c_w, can be measured similarly by dividing the distance of the transducer to the frontwall and back, $2D_{\mathrm{w}}$, by the round-trip time measured to the first echo, t_{Fw}. In this case, c_s can be found by dividing $2D_s$ by the time between the frontwall echo and the backwall echo, t_d.

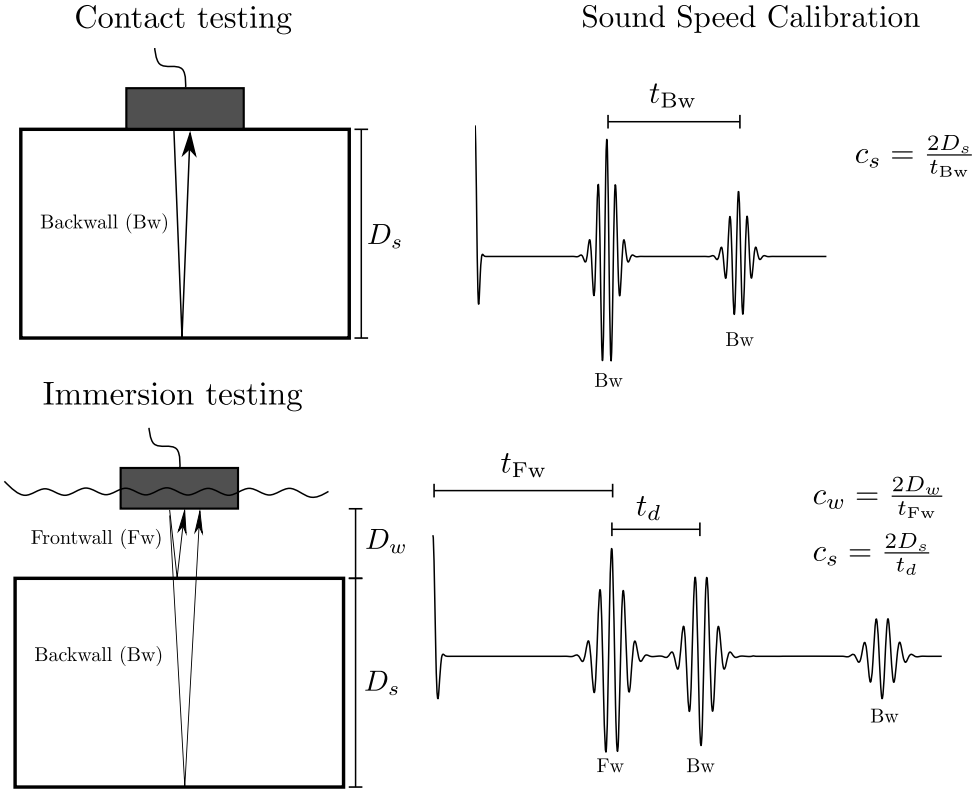

Source: Own authorship.

3.1 REFERENCE-FREE SOUND SPEED ESTIMATION

When no information is available about the geometry of the specimen, the distortion or blur level on reconstructed images may be used as an indication of speed mismatch. By defining a metric or function to quantify the sharpness of the reconstructed image, it is possible to search for the speed that maximizes the sharpness and thus assign it as the estimated speed. This process is analogous to the autofocus used in practically every modern digital camera (HE *et al.*, 2003; KO *et al.*, 2001). In this sense, the sound speed can be seen as a focusing parameter that can be tuned based on visual assessment of image sharpness.

Hunter *et al.* (2010a) proposed an autofocus method to estimate the position of the elements in a flexible array by maximizing the contrast of the reconstructed image. The main limitation of their method is that the image must contain an isolated feature. Although this limitation has been addressed in another work (HUNTER *et al.*, 2011), the scheme is still based on strong assumptions of the features present in the image, e.g. a planar backwall.

Napolitano *et al.* (2006) developed a method to automate the sound speed selection in order to increase lateral resolution in the resulting image. This is done by analyzing the spatial frequency data of images reconstructed with various sound speeds.

This concept was also applied to photoacoustic tomography of living tissues (TREEBY *et al.*, 2011) in order to obtain an average sound speed that maximizes image sharpness. The authors investigated the use of three image quality metrics in an interval ranging from 1400 m/s to 1600 m/s. This class of methods eliminates the need of prior knowledge, such as the geometry of a calibration block, or a reference for comparison, such as a ground-truth image. Therefore, this class may be denoted as reference-free.

Jakovljevic *et al.* (2018) proposed a model-based local sound speed estimator. This estimator uses an inverse problem approach to evaluate the local sound speeds from the average sound speed in a given path. The average sound speed is obtained using the method by (ANDERSON *et al.*, 2000), where a wire target is imaged with varying beamforming parameters, i.e., varying assumed sound speeds.

Abe *et al.* (2019) proposed a method to fit the theoretical propagation time from a known scatterer to each probe element with the measured values, in order to estimate the sound speed distribution. Their method requires knowledge of scatterer location in order to evaluate the theoretical propagation times.

In (MOURA *et al.*, 2020) it was proposed a method to estimate the sound speed similar to the one presented in (TREEBY *et al.*, 2011). The method, which also evaluates a metric over reconstructed images, requires a fine grid in order to obtain the extremum of the metric function. This requires many images to be reconstructed and, thus, the method is time-consuming.

3.2 IMAGE QUALITY METRICS

The literature of IQA is abundant in methods for determining focus, presence of artifacts and general quality of images, according to the human perception (WANG *et al.*, 2002a; WANG, 2011). These methods are usually grouped in three categories: Full-Reference, Reduced-Reference and No-Reference. The first category compares a distorted image to a reference image to evaluate the quality. In a Reduced-Reference scheme, there is no reference image but there is information about the characteristics of the reference image, e.g., some statistical model (D.V.M; SIMONCELLI, 2005). In the No-Reference case, there is only the distorted image and the distortion is assumed to follow a model, for example, a gaussian blur (WANG *et al.*, 2002b).

The mismatch between the assumed and actual speeds causes distortions in the reconstructed images. Without a reference image of the specimen, No-Reference metrics allow this distortion to be used as a means to estimate the mismatch between speeds. Hereinafter, the term "metric" refers to No-Reference metrics and the goal is to determine the value for which the mismatch is closer to zero.

Treeby *et al.* (2011) employed three metrics: Brenner gradient, Tenenbaum gradient and normalized variance. Hunter *et al.* (2010a) employed the contrast of reconstructed images as a quality metric. The authors used an autofocus approach to estimate the positions of the transducer elements in a flexible array by maximizing the contrast of the reconstructed images. In this study, the application of these functions in an autofocus approach to speed estimation in NDE is verified.

Since there are many possible choices for metrics, here only the more relevant metrics found in the NDE literature will be used. The first metric, the Tenenbaum gradient (TREEBY *et al.*, 2011), can be posed as

$$F_g = \sum_{x,z} \left[(g * I)^2 + (g^T * I)^2 \right]_{x,z} \quad , \tag{6}$$

where x and z are the horizontal and vertical indices of the image, $*$ denotes the 2-D convolution operator, I represents the image and g can be defined as the Sobel Operator

$$g = \begin{bmatrix} -1 & 0 & 1 \\ -2 & 0 & 2 \\ -1 & 0 & 1 \end{bmatrix}. \tag{7}$$

The Brenner gradient presented in (TREEBY *et al.*, 2011) was not included as it is very similar to Tenenbaum gradient and presents worse performance as estimatior (TREEBY *et al.*, 2011).

The normalized variance is calculated as

$$F_v = \frac{1}{\mu} \sum_{x,z} (I(x,z) - \mu)^2, \tag{8}$$

in which $I(x,z)$ denotes the pixel with coordinates x and z and μ represents the mean pixel value of the image defined as $\frac{1}{N} \sum_{x,z} I(x,z)$ for an image of N pixels.

The next metric is the contrast of the image, defined as

$$F_c = \frac{\frac{1}{N} \sum_{x,z} (I'(x,z))^2}{\mu^2}, \tag{9}$$

where I' is the normalized image

$$I'(x,z) = \frac{I(x,z) - I_{\min}}{|I_{\max} - I_{\min}|} \quad . \tag{10}$$

The contrast lies in the range $[1,\infty)$ and is not defined for images that are zero everywhere.

The metrics presented will provide a single value for each image, which quantifies the image sharpness. These values can then be compared to evaluate which image is sharper and, thus, is associated with lower mismatch in assumed sound speed.

3.3 EXTREMUM SEARCH

A common approach to find the extremum of a function consists in searching for a zero in the gradient of the function. Considering a function $f(c)$ that returns the metric on a reconstructed image with sound speed c, the determination of the gradient $f'(c)$ is difficult, at best. Fortunately, there are methods to find extrema that do not require the evaluation of a gradient.

The method presented in (MOURA *et al.*, 2020) showed that for TFM images, the Tenenbaum function presented an unique maximum inside the search interval. In order to achieve

a precise estimation with a grid search, the search must be done over a fine grid. This requires a greater number of images to be reconstructed. Depending on the image size, this process becomes very time consuming.

When using a grid search, given the search interval $[a,b]$ and a step, t, the method requires $N_{gs} = \frac{(b-a)}{t}$. One way to reduce the number of images needed is to make use of a more sophisticated search method. One such method is the Golden Section Search (GSS) algorithm, which is used for finding an extremum inside an interval. The GSS algorithm takes approximately (BRENT, 2013, Chapter 5) $N_{gss} \cong 1.44 \log_2 \left(\frac{b-a}{t}\right)$, which makes it a more appropriate choice than the grid search. GSS has guaranteed convergence but, albeit better than the grid search, it is not the fastest method of extremum search.

The Successive Parabolic Interpolation is another method for finding an extremum. As the name suggests, it successively fits parabolas to the function using three points inside the interval. This method presents superlinear rate of convergence when it converges. Unfortunately, convergence is not guaranteed. If, for example, the three points selected are collinear, the fitted parabola is degenerate and the method fails.

Another method is the Brent's Minimum Search Method (BRENT, 2013, Chapter 5). For unimodal[1] functions of one variable, the method approximates the minimum in the search interval, up to a given tolerance, with guaranteed convergence. The algorithm can be easily adapted to find the maximum of a function.

Brent's method combines the robustness of GSS with the superlinear rate of convergence of the Successive Parabolic Interpolation. Whenever possible, the algorithm uses a parabolic interpolation step to accelerate convergence and, if the parabola is not acceptable, it uses a GSS step. The algorithm is detailed in Algorithm 1.

Figure 16 shows an example of finding the minimum of a function using Brent's method for an arbitrary function. The search interval is defined as [-40, 20] with a tolerance of 0.01, that is, the difference between the two last steps is smaller than, or equal to, the tolerance. In order to achieve this tolerance, the grid search method requires 6000 function evaluations while Brent's method requires only 13 evaluations.

[1] In this context, f is defined as unimodal on $[a,b]$ if for all x_0, x_1 and $x_2 \in [a,b]$, $x_0 < x_1 \wedge x_1 < x_2 \supset$ $\supset (f(x_0) \leq f(x_1) \supset f(x_1) < f(x_2)) \wedge (f(x_1) \geq f(x_2) \supset f(x_0) > f(x_1))$. So, for some unique $\mu \in [a,b]$, f is either strictly monotonic decreasing on $[a, \mu)$ and strictly monotonic increasing on $[\mu, b]$, or strictly monotonic decreasing on $[a, \mu]$ and strictly monotonic increasing on $(\mu, b]$ (BRENT, 2013).

Algorithm 1 – The pseudocode for estimating sound speed using Brent's Method (BRENT, 2013). $\Phi(\cdot)$ denotes the metric function that takes an image as input and $\mathbf{f}_I(\cdot)$ denotes the imaging function that takes the sound speed as input.

Require: $\Phi(\cdot)$, $\mathbf{f}_I(\cdot) \in \mathbb{R}^{N\times N}$, a, b and $t \in \mathbb{R}$
Ensure: $k = \frac{3-\sqrt{5}}{2}$, $e = 0$, $\epsilon = 0.5\sqrt{\epsilon_{machine}}$
$v = w = x = a + k(b - a)$
$\Phi_v = \Phi_w = \Phi_x = \Phi(\mathbf{f}_I(x))$
$m = 0.5(a + b)$
$tol = \epsilon|x| + t$
$tol_2 = 2tol$
while $|x - m| > tol_2 - 0.5(b - a)$ **do**
  $p = q = r = 0$
  if $|e| > tol$ **then**
    {Fit a parabola}
    $r = (x - w)(\Phi_x - \Phi_v)$; $q = (x - v)(\Phi_x - \Phi_w)$
    $p = (x - v)q - (x - w)r$; $q = 2(q - r)$
    if $q > 0$ **then** $p = -p$ **else** $q = -q$
    $r = e$; $e = d$
  end if
  if $|p| < |0.5qr|$ and $p < q(a - x)$ and $p < q(b - x)$ **then**
    {"Parabolic Interpolation" step}
    $d = p/q$; $u = x + d$
    if $u - a < tol_2$ or $b - u < tol_2$ **then**
      if $x < m$ **then** $d = tol$ **else** $d = -tol$
    end if
  else
    {"Golden Section" step}
    $e = b$ **if** $x < m$ **else** $e = a$
    $d = k.e$
  end if
  if $|d| \geq tol$ **then**
    $u = x + d$
  else
    if $d > 0$ **then** $u = x + tol$ **else** $u = x - tol$
  end if
  $\Phi_u = \Phi(\mathbf{f}_I(u))$
  if $\Phi_u \leq \Phi_x$ **then**
    if $u < x$ **then** $b = x$ **else** $a = x$
    $v = w$; $\Phi_v = \Phi_w$; $w = x$; $\Phi_w = \Phi_x$; $x = u$; $\Phi_x = \Phi_u$
  else if $\Phi_u \leq \Phi_v$ or $v = x$ or $v = w$ **then**
    $v = u$; $\Phi_v = \Phi_u$
  end if
  $m = 0.5(a + b)$
  $tol = \epsilon|x| + t$
  $tol_2 = 2tol$
end while
return x

Source: Brent (2013).

Figure 16 – Comparison of grid search and Brent's minimum search on an function. Both methods were given the same search interval, [-40, 20] and tolerance, 0.01. Grid search required 6000 function evaluations while Brent's method required only 13. The black cross states the initial function evaluation on Brent's method, a red cross indicates a GSS step while a green cross indicates a parabolic interpolation step.

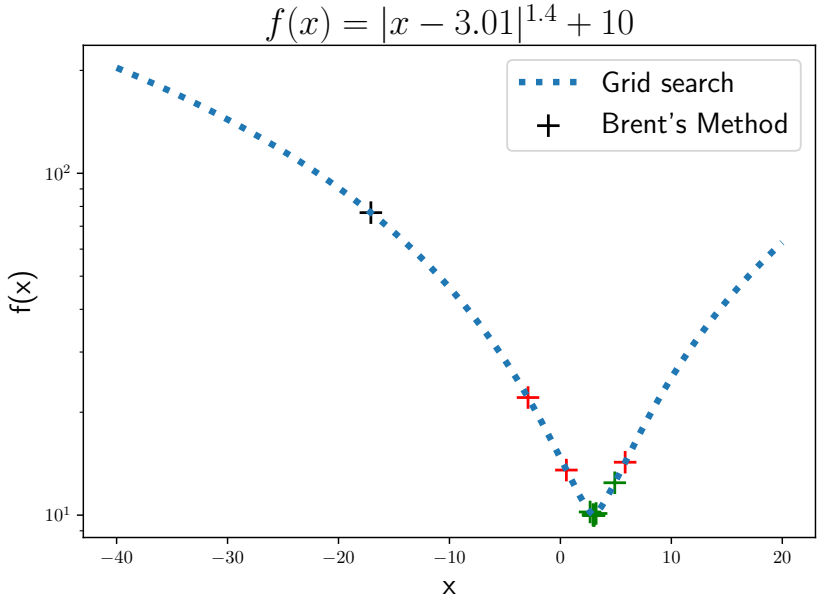

Source: Own authorship.

3.4 ESTIMATOR PERFORMANCE

One important consideration is that the image metrics will not always be smooth. This might cause the search methods to deviate from the true extremum. For Brent's method, this roughness in the image metrics might increase the standard deviation of the estimator. In this section, the impact of using Brent's method is analyzed and the results are compared to those obtained with grid search.

3.4.1 MSE of the Estimator

The use of simulated data is essential in evaluating the estimator performance, as with simulations it is easy to insert the required amount of Additive White Gaussian Noise (AWGN) for a given SNR level. After evaluation of signal power for the whole FMC, the noise power is determined according to desired SNR. The NDE simulation software CIVA (CIVA..., 2021) is capable of simulating a wide range of inspection scenarios, including: use of linear arrays, immersion inspections, configurable defects, specimen scanning, among others.

Using the NDE simulation software CIVA, a simple inspection scenario was designed in order to evaluate the performance of both grid search and Brent's method for distinct sound speeds. Also, the estimator performance under different levels of noise, present in the captured signals, must be evaluated.

The simulated object consists of a block, of generic material, of dimensions 80x60x24 mm with a single SDH in it. The sound speed in this material was set to two distinct values, first 4000 m/s then 6000 m/s. This is the same as simulating two different materials. The SDH included in the simulation has 1mm diameter and is located at 40mm depth with equal spacing to both sides, as illustrated in Figure 17. The ROI is defined as a 20x20 mm region, or 200x200 pixels, centered at the SDH. Images of this region were created using TFM. The transducer simulated is a model of Olympus 5L64-A32. Relevant information is summarized in Table 1.

The first step to evaluate the practicality of the estimator is to compare it against the grid search method. This helps in defining a baseline performance for further experiments.

Figure 17 – Simulated specimen used for measurement of estimator performance. The ROI is centered around the SDH and has dimensions 20x20 mm. For each dimension, the density of points is 0.1 mm/pixels.

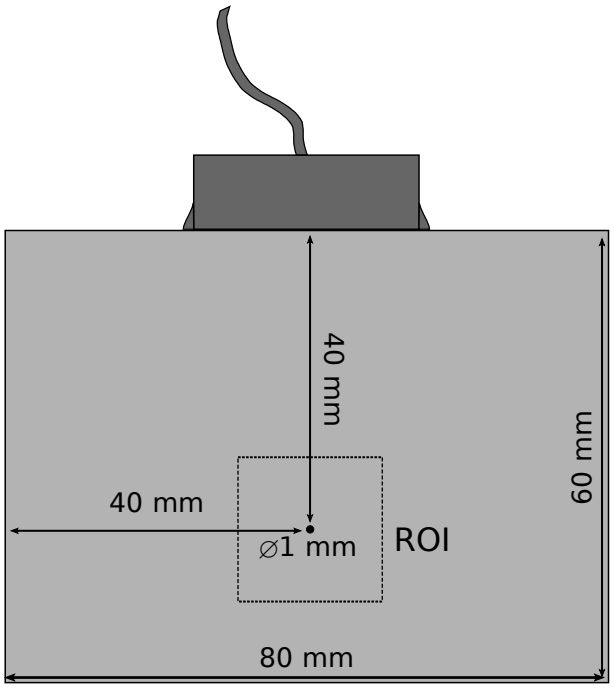

Source: Own authorship.

Table 1 – Parameters for the transducer Olympus 5L64-A32.

Parameter	Value
Central Frequency (MHz)	4.9
Bandwidth	50%
Number of elements	64
Element Pitch (mm)	0.5
Inter element space (mm)	0.02
Element Length (mm)	10

Source: Nova... (2021)

In order to evaluate the performance of an estimator, the first metrics that come to mind are bias and variance. The bias is defined as

$$b = \mathrm{E}\{\hat{c}\} - c, \tag{11}$$

where $\mathrm{E}\{\hat{c}\}$ denotes the expected value of the estimator and c denotes the true value. The variance of the estimator is defined as

$$\sigma^2 = \mathrm{E}\{(\hat{c} - c)^2\}. \tag{12}$$

Another metric is the MSE, that combines bias and variance in a single value. A single valued metric facilitates the evaluation of performance. The MSE is defined as

$$\mathrm{MSE} = b^2 + \sigma^2. \tag{13}$$

For this evaluation, the search interval was defined to lie between 90% and 110% of the true speed. For both methods the tolerance was set to 0.1 m/s, which for the grid search defines a uniform grid with a step of 0.1 m/s.

Table 2 shows the results obtained using the approach in (MOURA *et al.*, 2020) and using Brent's Method in four scenarios. Each combination of metric and method was evaluated over 500 trials, using different noise realizations, in order to obtain these results.

In this analysis, as expected, Brent's method required at most 23 steps to reach the desired tolerance. It also presented lower MSE than the grid search in the most cases. One possible explanation is that the Parabolic Interpolation step of Brent's Method has a smoothing effect over the metric function. The decrease in SNR presented small changes in bias and a higher effect on σ.

3.4.2 Uncertainty Analysis

Another important analysis to do is the uncertainty analysis. In order to do it, consider a typical configuration for estimating the sound speed in steel, $c = 5900$ m/s, with a specimen as the

Table 2 – Results of the sound speed estimator, using both search methods, in a simple simulated scenario. These were obtained after 500 trials in data embedded in AWGN. Differently from what was expected, the performance was increased with use of Brent's Method. Also, the Contrast metric performed a lot better, surpassing the performance of the Tenenbaum metric.

True Speed 4000m/s		Grid Search			Brent's Method		
		Tenenbaum	Variance	Contrast	Tenenbaum	Variance	Contrast
40dB	Bias (m/s)	8.01	24.66	34.04	10.19	8.20	**7.73**
	σ (m/s)	4.31	4.79	7.05	**0.44**	2.85	0.97
	MSE	82.74	631.06	1208.42	104.03	75.36	**60.69**
25dB	Bias (m/s)	8.37	16.65	16.47	9.17	8.64	**7.51**
	σ (m/s)	9.87	7.17	9.50	**1.15**	2.98	1.45
	MSE	167.47	328.63	361.51	85.41	83.53	**58.50**
True Speed 6000m/s							
40dB	Bias (m/s)	**12.38**	38.30	44.66	16.77	20.05	-18.85
	σ (m/s)	5.43	5.00	9.78	0.99	**0.28**	6.74
	MSE	**182.75**	1491.89	2090.16	282.21	402.08	400.75
25dB	Bias (m/s)	**9.78**	72.09	90.49	16.37	19.68	-18.07
	σ (m/s)	8.07	6.78	6.40	**0.96**	1.54	6.75
	MSE	**160.77**	5242.94	8229.4	268.90	389.67	372.09

Source: Own authorship.

one in Figure 17 and measurement noise added to the simulated signals with SNR level of 43 dB. This SNR level is compatible with the Panther acquisition system used in later experiments.

The relative combined uncertainty μ_r (JCGM, 2008) was evaluated for TFM images using all metrics. It is defined as

$$\mu_r = \frac{\mu_c}{\bar{c}}, \tag{14}$$

in which $\bar{c}$ denotes the mean value obtained in N estimates of sound speed and μ_c is the standard combined uncertainty. For simplicity, only the repeatability uncertainty was considered, leading to

$$\mu_c = \mu_n = \sigma(\bar{c}) = \sqrt{\frac{1}{N-1}\sum_{n=1}^{N}(c_n - \bar{c})}. \tag{15}$$

The values obtained for this configuration are summarized in Table 3. These values suggest that the Tenenbaum metric works best as it presents lower uncertainty. It also shows that the uncertainty increases with the use of Brent's method, with the exception of the contrast metric.

Table 3 – Relative uncertainty for the different variations of the method.

Grid Search	Tenenbaum	Variance	Contrast
μ_r (for steel - 5900 m/s)	**0.0166**%	0.0241%	0.0785%
Brent's Method	Tenenbaum	Variance	Contrast
μ_r (for steel - 5900 m/s)	**0.0571**%	0.112%	0.0795%

Source: Own authorship.

3.5 EXPERIMENTS

To demonstrate the efficacy of the Brent's method in more realistic scenarios, a series of experiments were realized. Objects of distinct materials were inspected by both contact and immersion, in order to estimate the sound speeds in each material.

All objects were inspected using an M2M Panther^{TM} (Eddyfi NDT, Inc.) Acquisition System with a 5L64-A32 transducer from Olympus described in Table 1. For each specimen used, sound speed was calibrated using the procedure shown in Figure 15. The search interval used was from 90% to 110% of the calibrated speed and the tolerance was set at 0.1 m/s.

The first experiment is done on an aluminum block, with the same dimensions of the one described in Figure 17. The sound speed in this block is 6319 m/s. The ROI used in the method was set to include the SDH and the backwall. Also, it was set to have 0.1 mm/pixels. The results are compared to those obtained using grid search and presented in Table 4. Although grid search obtained the best estimate with Tenenbaum metric, results with Brent's search method and Tenenbaum beat all other combination.

Table 4 – Sound speed estimation results using both search methods. The estimates using Brent's method presented higher error than the grid search estimates. Still, the Tenenbaum metric with Brent's method has lower error than the other metrics combined with grid search.

Estimated Speeds (m/s)	Tenenbaum	Error	Variance	Error	Contrast	Error
Grid Search	**6305.00**	**-14.00**	6299.00	-20.00	6197.00	122.00
Brent's Method	6301.74	-17.26	6298.04	-20.96	6201.57	117.43

Source: Own authorship.

A second experiment was done using an acrylic specimen, illustrated in Figure 18. As in the previous experiment, the inspection was done by contact with the transducer positioned at x =90 mm. The ROI had dimensions 40 mm×25 mm and was centered at (90, 17.5).

Figure 18 – Acrylic specimen with calibrated sound speed of 2767 m/s and triangular cuts along the backwall. The probe is positioned in a single location between the smallest and the largest cut. The ROI has dimensions 40 mm×24 mm and is positioned 5mm below the center of the probe, this ensures that the backwall is fully imaged for the entire search interval.

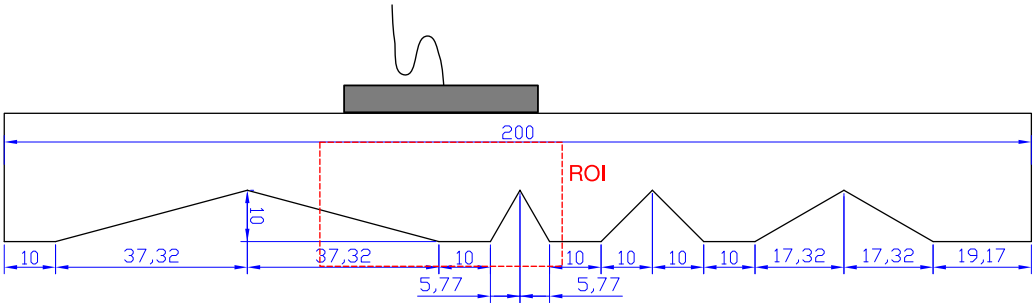

Source: Own authorship.

The results of this experiment using Brent's method also were compared to grid search. This time, Brent's method paired with any metric presented better estimates.

Table 5 – Sound speed estimation on an acrylic specimen using both search methods. The estimates using Brent's method presented better agreement with the measured value of 2767 m/s.

Estimated Speeds (m/s)	Tenenbaum	Error	Variance	Error	Contrast	Error
Grid Search	2731.86	-35.14	2737.12	-29.86	2731.86	-35.14
Brent's Method	2762.02	-4.98	**2764.40**	**-2.60**	2787.22	20.22

Source: Own authorship.

Another experiment with an acrylic specimen was done, this time with a curved specimen as illustrated in Figure 19. Because of its shape, this object was inspected by immersion. Therefore, the sound speed in water and in the acrylic were both estimated. The first step was to find the sound speed in water using all metrics. The second step consisted in estimating the sound speed in the acrylic using the estimates from the first step. That is, to reconstruct an image inside the specimen, the sound speed in water must be considered.

Figure 19 – Drawing of the acrylic curved specimen inspected, the dimensions are in millimeter. This design is inspired on a corroded pipeline. The calibrated sound speed in the specimen is 2767 m/s. The acrylic specimen will be inspected inside a water tank with an approximate water path of 33 mm, with the center of the array over the center of the specimen. The ROI used for estimating the sound speed in water is represented by ROI 1 and the ROI for estimating the sound speed in the object is represented by ROI 2, in red.

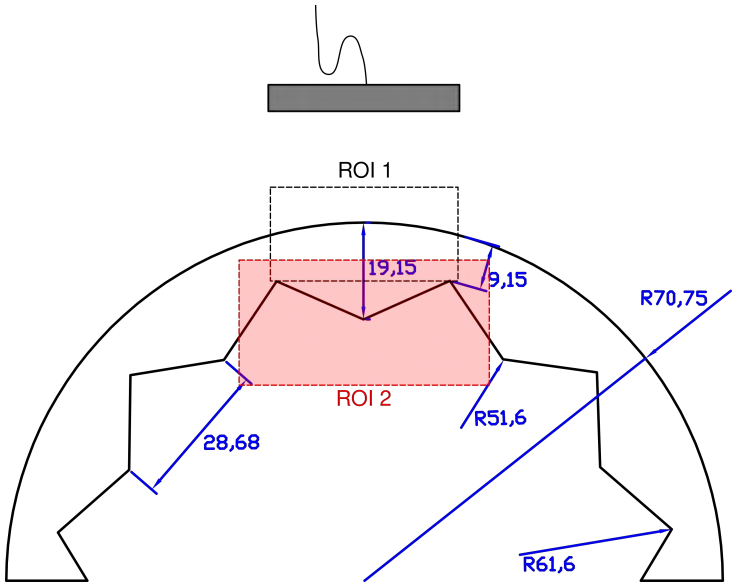

Source: Own authorship.

In this experiment, the transducer was positioned approximately 35 mm above the specimen. For estimating the sound speed in water, the ROI was defined with dimensions 30x15 mm and centered at (0 mm, 37.5 mm). For the sound speed in the specimen, the ROI was defined with dimensions 40 mmx20 mm and centered at (0, 45). The estimates using both search

methods are compared in Table 6. The estimates using grid search were worse for sound speed in water but better in acrylic.

An issue that arises here is that the ROI must not contain the external surface of the object. As the surface will not change position when varying the sound speed in the specimen, it will dominate the image and the estimation will fail. One possible way to bypass this, is to mask the image in the external surface region. This is considered for future works.

Table 6 – Sound speed estimation on an acrylic curved specimen using both search methods. The estimates for sound speed in water presented small changes between the search method, the exception being the estimates with the contrast metric. For the sound speed in the specimen, grid search estimates are more accurate.

Estimated Speeds (m/s) Water - 1481 m/s	Tenenbaum	Error	Variance	Error	Contrast	Error
Grid Search	1487.07	6.07	1490.03	9.03	1776.02	295.02
Brent's Method	**1486.21**	**5.21**	1488.73	7.73	1494.64	13.64
Acrylic - 2767 m/s						
Grid Search	2727.99	-39.01	2749.01	-17.99	**2750.95**	**-16.05**
Brent's Method	2725.15	-41.85	2734.10	-32.90	2727.78	-39.22

Source: Own authorship.

The difference between estimates for sound speed in water using the contrast metric, along with grid search, is caused by the contrast metric having a local maximum close to the calibrated speed and not a global maximum. Brent's method is drawn to this local maximum, thus finding a better estimate. This is shown in Figure 20.

Figure 20 – Metric curves for sound speed estimation in water obtained using grid search with step size of 1 m/s. Curves for Tenenbaum and variance present clear advantage over the contrast metric, which has a maximum at the upper end of the interval.

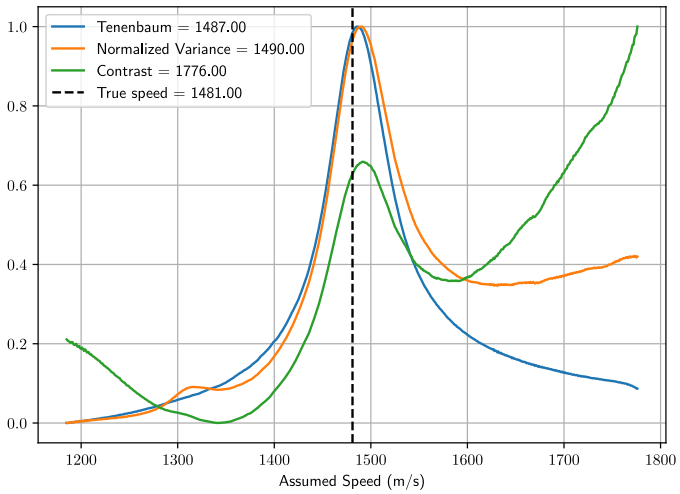

Source: Own authorship.

3.6 SPECKLE PATTERN

An exploratory experiment was done, in order to evaluate how speckle pattern would affect the sound speed estimation process. Speckle pattern is a granular pattern that appears in ultrasound images. It is caused by a coherent sum of echoes from scatterers too small to resolve (WELLS; HALLIWELL, 1981). These scatterers are randomly distributed and with random amplitudes. Because of that, this pattern is sometimes referred as *speckle noise*.

Given that these small scatterers and the probe remain stationary, the speckle pattern will remain fixed. As it is, this pattern cannot be removed simply by taking the mean of several images as is done for random noise. There are methods in the literature that deal with speckle pattern removal, or *despeckle*, to cite a few (LI *et al.*, 1992; ABD-ELMONIEM *et al.*, 2000; NARAYANAN; WAHIDABANU, 2009).

More recently, some authors have proposed that the speckle pattern brings important information that can help in a medical diagnosis (NARAYANAN; WAHIDABANU, 2009) or be used in motion tracking (LIANG *et al.*, 2013).

As the speckle pattern arises from the imaging process, the same way as the discontinuities, it is possible to use it for the purpose of speed estimation. An additional experiment was done in order to evaluate the efficacy of the proposed method on images containing only speckle. Figure 21 illustrates one such image where only speckle is present.

Figure 21 – Example of an image containing only speckle in a region of the specimen.

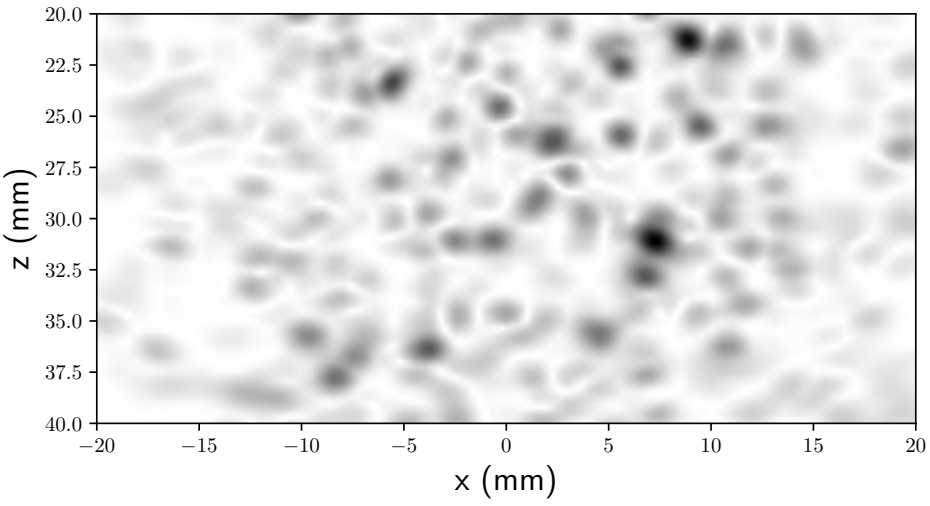

Source: Own authorship.

For this analysis, an inspection of a steel block (sound speed 5900 m/s) without any flaw was simulated. The scatterers are placed using CIVA's option of "Structural Noise", with density 0.1 pts/mm^3 and amplitude of 1 S.I. as parameters. Images of this specimen were created using TFM with a ROI of 30x10 mm and 0.1 mm/pixels. As the position of small scatterers is randomly distributed, the ROI was also randomly shifted around the center of the block cross-section for each trial. These shifts were done in order to evaluate sound speed in different regions.

In total, 1000 trials were done and the MSE obtained with each method are summarized in Table 7. From these results, it is clear that although bias is similar to the results in Table 2, the standard deviation is much higher. One possible explanation to these is that some of the random positions of the ROI might have important features near the borders. Depending of the assumed speeds, these features might be located outside the reconstructed image. This would cause abrupt differences in the metrics curves and, possibly, lead to wrong estimates.

Table 7 – Estimator error when the images contain only speckle. Clearly, the Tenenbaum metric provides much better estimates even if inferior to other scenarios. The foremost issue with these estimates is the high standard deviation, σ.

Speckle density 0.1 pts/mm^3	Tenenbaum	Variance	Contrast
Bias (m/s)	13.42	34.15	-19.96
σ (m/s)	**37.93**	55.35	87.04
MSE	1618.78	4229.85	7974.36

Source: Own authorship.

3.7 COMMENTARIES

Two reference-free methods for sound speed estimation were proposed. The method proposed in (MOURA *et al.*, 2020) uses grid search in order to find the metric functions extremum. This search method requires a fine grid and therefore the reconstruction of many images. By using the Brent's method, as proposed here, the time required to make an estimate is greatly reduced while the performance is not much affected. Also, the practicality of the method was demonstrated for images containing the backwall, flaws and even speckle, either together or isolated.

The relative uncertainty of the method was evaluated for the three metrics. For the Tenenbaum metric, it was found to be as low as 0.0571%. Although higher than the value found using grid search, it is still lower than the values found for the contrast metric. The uncertainties were found using simulations, therefore the values can only be considered as baselines.

The contributions of the studies presented here are three:

- Reference-free sound speed estimation using grid search (MOURA *et al.*, 2019; MOURA *et al.*, 2020).
- Reference-free sound speed estimation using Brent's method.
- Reference-free sound speed estimation based on speckle pattern.

Future works include: (1) development of a metric using machine learning methods, in order to optimize the estimation process; and (2) development of a reference-free method for estimating direction-dependent sound speed in anisotropic materials.

4 SURFACE ESTIMATION VIA ANALYSIS METHOD (SEAM)

In many applications of ultrasound in NDE, one needs to image structures with non-planar surfaces. A common way to accomplish that is to have the transducer coupled to a solid shoe that conforms to the inspected structure. Although simple, this approach requires a different shoe for each surface.

Approaches that are more flexible were also designed, such as surface adaptive transducers (HUNTER *et al.*, 2010a; HUNTER *et al.*, 2010b). In similar fashion, water can be used as couplant, either by immersing the structure or via a water filled membrane (RUSSELL *et al.*, 2012).

Independent of how the transducer is coupled to the surface, in order to produce interior images with methods such as TFM (HOLMES *et al.*, 2004; HOLMES *et al.*, 2005), the ray paths through the surface to points inside the specimen must be calculated. When the surface is not known beforehand, it must be estimated prior to interior imaging.

Camacho *et al.* (2014) proposed a method to extract the surface from A-scans captured using pulse-echo, pitch-catch and plane-waves schemes with a linear array probe. This method was reported to be robust when the surface under inspection is of convex shape with relatively small curvature radius.

Other approaches (LE JEUNE, L. *et al.*, 2015; ZHANG *et al.*, 2014; MCKEE *et al.*, 2020) consist in applying TFM to the coupling medium (water, rexolite, etc.) and identifying the surface by the image. LE JEUNE, L. *et al.* (2015) identified the surface points by taking the maximum value of each column in the image and applying a moving average filter to smooth the profile.

Malkin *et al.* (2018) proposed a scheme for extracting the surface profile after acquiring the FMC data with a linear array and scanning over a specimen. First, the TFM images obtained at each position are stitched together. Then, the first peak with amplitude surpassing a certain threshold in each column of the image is taken as a surface point. This threshold is defined as the median pixel value in the surface region.

More recently, McKee *et al.* (2020) proposed a method for estimating the surface in a 3D setting. The methods first step is to generate an stitched 3D TFM image of the surface, considering only the coupling medium. From the images, the surface is iteratively identified.

The common ground of these approaches is that the first step is to generate a TFM image considering a single medium, i.e., the coupling medium. The method proposed herein shares some of the steps done in the other approaches but greatly differs in how to treat the measurements for noise. This method is based on a constrained inverse problem, much like denoising, and is more robust to image noise than others found in the literature.

4.1 INVERSE PROBLEM BASED SURFACE ESTIMATION

The first step to extracting the surface is to obtain an image of the surface considering a single medium, e.g., water. This can be done with any imaging algorithm like SAFT, TFM or CPWC. The choice for TFM imaging is justified as it will also be used for imaging inside the specimen. The method is formulated using the TFM algorithm and a linear array for 2D imaging, but this can be easily extended to a matrix array and 3D imaging.

This image, reconstructed considering only the coupling medium, will provide an initial estimate, $\check{\mathbf{z}}$, of the surface profile. As done in (LE JEUNE, L. *et al.*, 2015), the initial estimate is taken as the pixel of maximum intensity of each column of the image. If there is more than one position with the maximum value, the first one is considered. In some cases, the surface will contain sections that reflect the waves away from the transducer. This will cause these sections to have lower intensities in the image, as illustrated in Figure 22.

To provide a better estimate of the surface profile, an inverse problem is formulated as

$$\hat{\mathbf{z}} = \arg\min_{\mathbf{z}} F(\mathbf{z} - \check{\mathbf{z}}) + G(\mathbf{z}), \tag{16}$$

in which $F(\cdot)$ is intended to approximate the estimate, $\mathbf{z}$, to the initial estimate $\check{\mathbf{z}}$. The choice for $F(\cdot)$ should, ideally, take into account the distribution of $\mathbf{r} = \mathbf{z} - \check{\mathbf{z}}$. For example, if $\mathbf{r}$ is Gaussian distributed, then the ℓ_2-norm would be the best choice so that $F(\mathbf{r}) = \frac{1}{2}\|\mathbf{z} - \check{\mathbf{z}}\|_2^2$.

The ℓ_2-norm is a convenient choice even if $\mathbf{r}$ is not Gaussian distributed. The function is convex, smooth and there are many tools already developed to minimize it. If the distribution of $\mathbf{r}$ can be approximated by a Gaussian, then the ℓ_2-norm is a valid choice.

The second term, $G(\mathbf{z})$, is used to include prior knowledge of the solution into the problem. The Total Variation (TV) seminorm (RUDIN *et al.*, 1992; CHAN *et al.*, 2001) is a very popular choice (CHAMBOLLE, 2005) for $G(\cdot)$ in signal denoising/reconstruction problems.

Figure 22 – Image of a simulated inspection of the backwall of a specimen. Pixels with amplitude lower than -36dB were omitted for greater clarity. The sides of the triangle in the backwall reflect waves away from the transducer, so that the echoes from these regions are not detected.

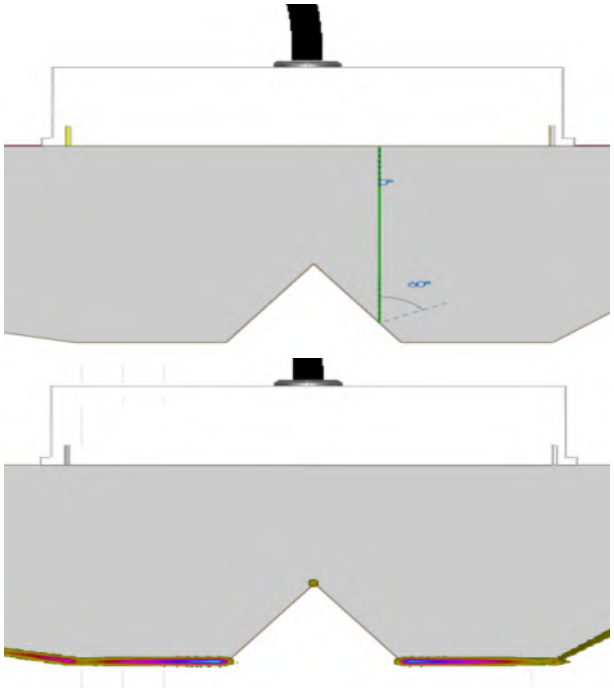

Source: Own authorship.

TV regularization is useful when the signal is expected to be piecewise constant. It acts as a low-pass filter that preserves edges. Total Variation for 1D signals is defined as

$$\mathrm{TV}(\mathbf{z}) = \tau \sum_i |z_{i+1} - z_i| = \tau \left\|\mathbf{Dz}\right\|_1 , \tag{17}$$

in which $\mathbf{D}$ denotes a first-order finite difference matrix and τ is the regularization parameter, that controls the compromise between the data fidelity and the regularization terms. The idea is to make the vector $\mathbf{Dz}$ sparse, thus, removing small variations from the signal and keeping only variations from discontinuities. The effects of TV regularization are illustrated in Figure 23.

Differently from the approach in (MALKIN *et al.*, 2018), that forces part of the surface to be linear by interpolation, the proposed approach does not force this on the solution. Regions of the surface that have curves are preserved as such, to a certain degree.

While a first-order finite difference operator promotes piecewise constant solutions, a higher-order operator promotes piecewise smooth solutions and avoids the staircase effect. Figure 23 shows an example of higher-order TV denoising, where the sharp edges of the original signal are maintained while slower transitions are smooth.

As the specimen's surface is not expected to be piecewise constant, a higher-order operator is desired. A second-order finite difference is then used to promote piecewise linearity

Figure 23 – Denoising piecewise linear or smooth functions using first-order TV usually lead to the staircasing effect. The use of higher-order TV eliminates the staircasing effect while maintaining sharp edges.

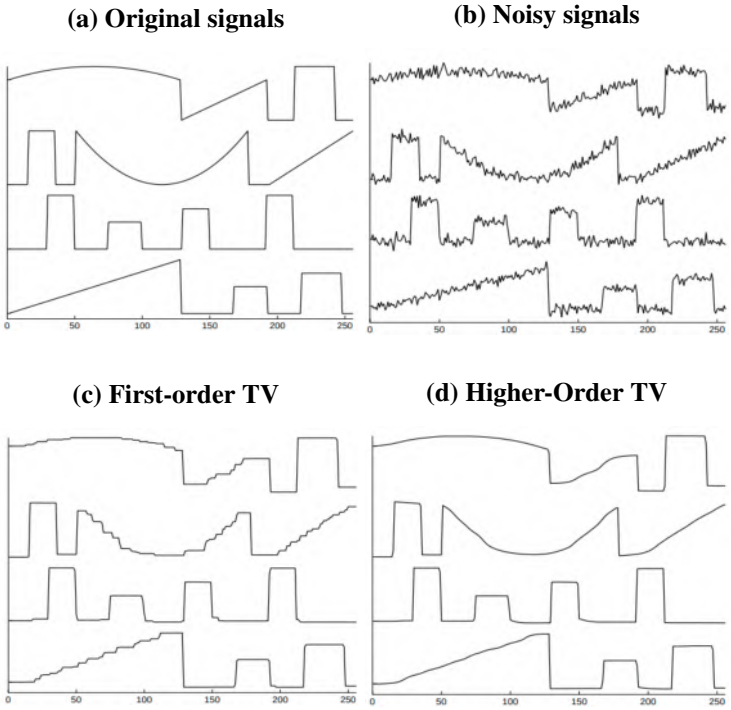

Source: Adapted from Chan *et al.* (2000).

in the estimated surface and will be denoted as $\mathbf{D}^2$. This way, Equation (16) becomes

$$\hat{\mathbf{z}} = \arg\min_{\mathbf{z}} \frac{1}{2} \|\mathbf{z} - \check{\mathbf{z}}\|_2^2 + \tau \left\|\mathbf{D}^2\mathbf{z}\right\|_1 . \tag{18}$$

The main issue in this formulation is that it applies the regularization to every part of $\mathbf{z}$ equally. Regions with higher SNR should not be penalized for not being linear the same way as regions with low SNR. The regularization parameter τ is used to weight the regularization term, in order to reduce noise in the solution. With this approach it is hard to tune τ, as the SNR is not constant along the whole TFM image. Figure 24 illustrates this difficulty. When τ is low, regions of higher SNR are kept but there is little noise suppression in regions of lower SNR. If τ is high enough to suppress noise adequately, it makes the overall profile over-smoothed.

One way to account for these different SNRs, is to change $F(\cdot)$ to the Weighted Least Squares (WLS). With this change, Equation (18) becomes

$$\hat{\mathbf{z}} = \arg\min_{\mathbf{z}} \frac{1}{2} \left\|\mathbf{W}^{\frac{1}{2}} (\mathbf{z} - \check{\mathbf{z}})\right\|_2^2 + \tau \left\|\mathbf{D}^2\mathbf{z}\right\|_1 , \tag{19}$$

in which $\mathbf{W}$ denotes the diagonal weighting matrix. This diagonality implies that the positions of the residue vector are uncorrelated. Ideally, the matrix $\mathbf{W}$ should be the inverse of the variance-covariance matrix of the observation (STRUTZ, 2016, Chapter 3).

Figure 24 – Example of surface estimation with TV regularization. A lower τ fails to suppress noise while keeping the high SNR regions intact. A higher τ removes noise from the estimate but makes the solution over-smooth.

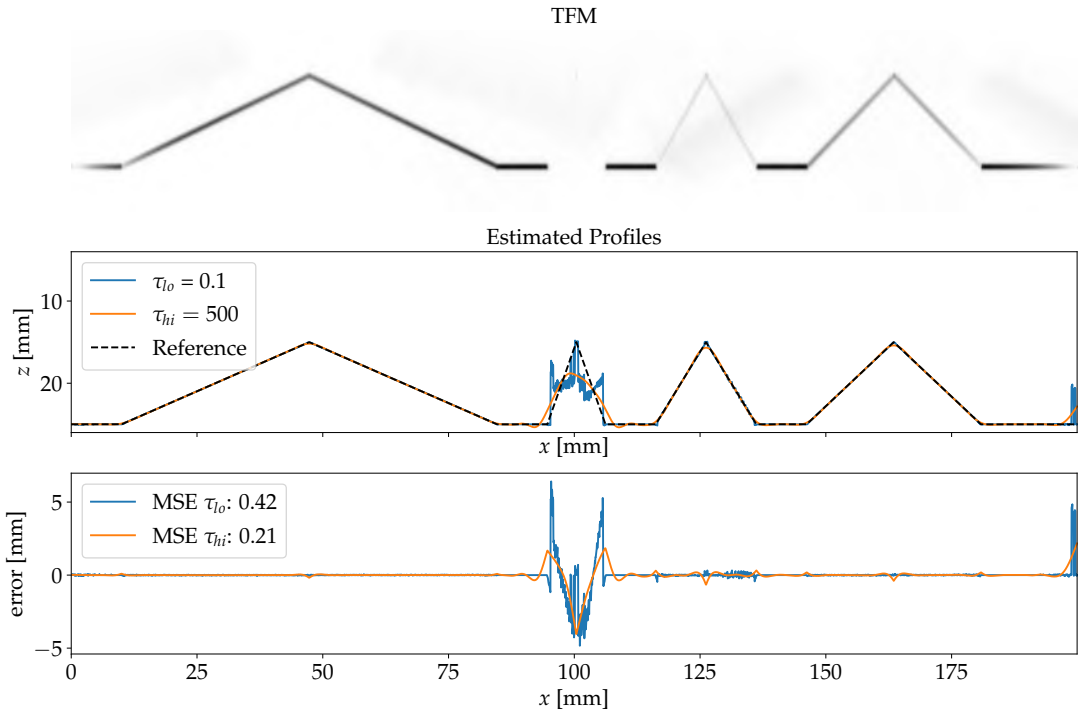

Source: Own authorship.

Equation 19 defines the objective of the proposed method. As the regularization term makes use of an sparsifying transform (the finite difference operator) this inverse problem falls into the analysis category (ELAD *et al.*, 2007). Thus, the method was named Surface Estimation via Analysis Method (SEAM).

Another interpretation to these weights is that they represent the confidence level in each point of the initial estimate. This way, the ℓ_2-norm will enforce lower differences where the confidence level is high. And if the confidence level in a region is low, the smaller weights will allow the final estimate to be different from the initial one. This allows the regularization term to have higher values without over-smoothing regions of high confidence and ensures that it promotes linearity in the low confidence regions.

As noted, matrix $\mathbf{W}$ should be the inverse of the variance-covariance matrix of the estimator $\check{\mathbf{z}}$. As shown in Appendix A, the variance of this estimator is not easily obtained. But, considering noise level as constant across the image, a reasonable approximation to the variance is the value of maximum amplitude for each column. Figure 25 illustrates the effect of these weights on the profile estimated with SEAM.

Figure 25 – Different elements of the SEAM algorithm. Top image shows the TFM image of the surface. Initial surface positions, ž, and weights, $\mathbf{W}^{\frac{1}{2}}$, are extracted from the TFM image. The estimated profile is obtained using SEAM.

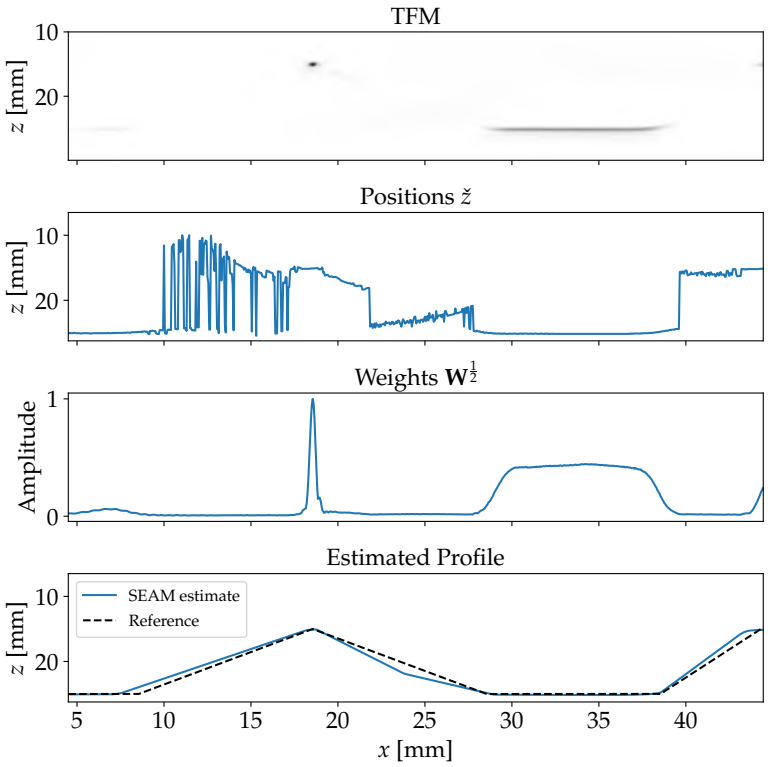

Source: Own authorship.

4.2 SOLVING THE INVERSE PROBLEM

To solve Equation (19), a fast implementation of the Alternating Direction Method of Multipliers (ADMM) algorithm was used. The algorithm, denoted fADMM (GOLDSTEIN *et al.*, 2014), uses the acceleration scheme first proposed in (NESTEROV, 1983) to improve the convergence rate of the algorithm. It also includes a restart condition that ensures stability in the case of a weakly convex[1] problem, such as the one in Equation (19).

In order to use the ADMM algorithm, first the problem needs to be cast as

$$\begin{aligned} \min \quad & F(\mathbf{z}) + G(\mathbf{y}) \\ \text{s.t.} \quad & \mathbf{Az} + \mathbf{By} = \mathbf{c}. \end{aligned} \tag{20}$$

[1] Given any two points, x_1 and x_2, and a real valued $\lambda \in [0,1]$, a ρ-convex function f satisfies: $f(\lambda x_1 + (1-\lambda)x_2) \leq \lambda f(x_1) + (1-\lambda) f(x_2) - \lambda(1-\lambda)\rho \|x_1 - x_2\|^2$.
If ρ is negative, then f is said to be weakly convex (VIAL, 1983).

By defining the following

$$F(\mathbf{z}) = \frac{1}{2}\left\|\mathbf{W}^{\frac{1}{2}}\left(\mathbf{z}-\check{\mathbf{z}}\right)\right\|_2^2$$

$$G(\mathbf{y}) = \tau\left\|\mathbf{y}\right\|_1$$

$$\mathbf{A} = \mathbf{D}^2$$

$$\mathbf{B} = -\mathbf{I}$$

$$\mathbf{c} = \mathbf{0},$$

problem (20) becomes

$$\begin{aligned} \min \quad & \frac{1}{2}\left\|\mathbf{W}^{\frac{1}{2}}\left(\mathbf{z}-\check{\mathbf{z}}\right)\right\|_2^2 + \tau\left\|\mathbf{y}\right\|_1 \\ \text{s.t.} \quad & \mathbf{D}^2\mathbf{z} = \mathbf{y}, \end{aligned} \tag{21}$$

which can be minimized separately for $\mathbf{z}$ and $\mathbf{y}$. The pseudocode for fADMM, used to solve Equation (21), is explained in Algorithm 2.

Algorithm 2 – The pseudocode using fADMM to solve Equation (19)**.**

Require: $\mathbf{W}, \mathbf{D}^2 \in \mathbb{R}^{N\times N}$, $\check{\mathbf{z}} \in \mathbb{R}^N$, and $\rho, \tau, \epsilon, \eta, K \in \mathbb{R}$
Ensure: $\hat{\mathbf{y}}_1 = \mathbf{0}$, $\hat{\mathbf{x}}_1 = \mathbf{0}$, $\mathbf{y}_0 = \mathbf{0}$, $\mathbf{x}_0 = \mathbf{0}$, $c_0 = 0$, $\alpha_1 = 1$, $r_0 = \infty$
$[S_a(\mathbf{b})]_i = \max(|\mathbf{b}_i| - a, 0) \cdot \frac{\mathbf{b}_i}{|\mathbf{b}_i|}$
for $(k = 1,2,3,...,K)$ **do**
  $\mathbf{z}_k = \left(\mathbf{W}^T\mathbf{W} + \rho(\mathbf{D}^2)^T\mathbf{D}^2\right)^{-1} \times \left(\mathbf{W}^T\mathbf{W}\check{\mathbf{z}} + \mathbf{D}^2(\rho\hat{\mathbf{y}}_k + \hat{\mathbf{x}}_k)\right)$
  $\mathbf{y}_k = S_{\tau/\rho}(\mathbf{D}^2\mathbf{z}_k - \hat{\mathbf{x}}_k/\rho)$
  $\mathbf{x}_k = \hat{\mathbf{x}}_k - \rho(\mathbf{D}^2\mathbf{z}_k - \mathbf{y}_k)$
  $c_k = \rho^{-1}\|\mathbf{x}_k - \hat{\mathbf{x}}_k\|^2 + \rho\|\mathbf{y}_k - \hat{\mathbf{y}}_k\|^2$
  if $c_k < \eta c_{k-1}$ **then**
    $\alpha_{k+1} = \frac{1+\sqrt{1+4\alpha_k{}^2}}{2}$
    $\hat{\mathbf{y}}_{k+1} = \mathbf{y}_k + \frac{\alpha_k - 1}{\alpha_{k+1}}(\mathbf{y}_k - \mathbf{y}_{k-1})$
    $\hat{\mathbf{x}}_{k+1} = \mathbf{x}_k + \frac{\alpha_k - 1}{\alpha_{k+1}}(\mathbf{x}_k - \mathbf{x}_{k-1})$
  else
    $\alpha_{k+1} = 1$, $\hat{\mathbf{y}}_{k+1} = \mathbf{y}_{k-1}$, $\hat{\mathbf{x}}_{k+1} = \mathbf{x}_{k-1}$
    $c_k \leftarrow \eta^{-1}c_{k-1}$
    $r_k = \|\mathbf{W}(\mathbf{z}_k - \check{\mathbf{z}})\|_2^2 + \tau\left\|\mathbf{D}^2\mathbf{z}_k\right\|_1$
  end if
  if $(r_k - r_{k-1}) \leq \epsilon$ **then**
    $n\_it = k$
  end if
end for
return $\mathbf{z}_k, r_k, n\_it$

Source: Own authorship.

The pseudocode for fADMM, with the changes to solve Equation (21), is given in Algorithm 2. The algorithm can be separated in four blocks:

- Initialization of parameters and auxiliary vectors and variables.

- Gradient descent steps: minimization with respect to both $\mathbf{z}$ and $\mathbf{y}$ is done in steps 3 to 6. $S_a(\cdot)$ denotes the shrinkage operator, defined in Step 1. Vectors $\hat{\mathbf{x}}_k$ and $\hat{\mathbf{y}}_k$ are intermediates used for the acceleration steps (8 to 10);

- Accelerated steps: The combined residual is denoted as c_k. If the inequality in step 7 is satisfied, then the acceleration steps (8 to 10) are taken.

- Restart steps: If the inequality (step 7) is not satisfied, steps 12 to 14 follow. These steps restart the acceleration and roll back vectors $\hat{\mathbf{x}}_k$ and $\hat{\mathbf{y}}_k$. The following iteration is not accelerated.

The method requires the definition of three parameters: ρ, τ, ϵ and η. The parameter η is used to control the frequency of restarts. Parameter ρ controls the size of the step taken in the gradient descent steps. The required convergence tolerance is defined as ϵ and presents a trade-off between accuracy and computation time. Among these parameters, only τ needs to be adjusted for different problems.

The computational burden of this method is higher than those proposed in (LE JEUNE, L. *et al.*, 2015) and (MALKIN *et al.*, 2018). However, since it can be accomplished faster than the imaging process, this should not limit its application.

4.3 SIMULATED SCENARIOS

In order to evaluate the accuracy of SEAM, simulations were carried out using the software CIVA. SEAM is compared to the method presented in (MALKIN *et al.*, 2018).

SEAM requires parameters τ, ρ and η. Parameter η is set to 0.999, as recommended in (GOLDSTEIN *et al.*, 2014), parameter ρ is set to 100 and parameter τ is set to 1 for every reconstruction from simulated data.

Both methods were used to estimate the bottom surface of an acrylic specimen, shown in Figure 26. The array was moved in order to scan the specimen at 25 positions, starting above the tip of the first triangle and, with uniform steps, towards the tip of the last triangle. The simulated FMCs were embedded in AWGN with an SNR of 40 dB. For each position, an image was formed using TFM and all images were stitched together to form a single image of the bottom surface. The final image is then scaled to have maximum pixel value of 1.

Figure 27 shows the TFM image along with the reference and estimated profiles. SEAM presented slightly higher MSE than Malkin's method. The fact that the geometry of the specimen

Figure 26 – Schematic of the acrylic specimen inspected and the probe's trajectory. The trajectory starts in $x = 45$ mm and goes to $x = 170$ mm in steps of 5 mm. At each position an FMC acquisition is done.

Source: Own authorship.

contains only straight lines, makes it easy for both methods to perform well. Even so, Figure 28 evidences that Malkin's method presents noise in the estimate whereas SEAM results in a line much closer to the reference.

Figure 27 – Surface estimation in a simulated scenario with an SNR level of 40 dB. The bottom surface was estimated using SEAM and the one by Malkin *et al.* (2018). Both methods present good agreement with the reference profile but SEAM presents slightly worse MSE.

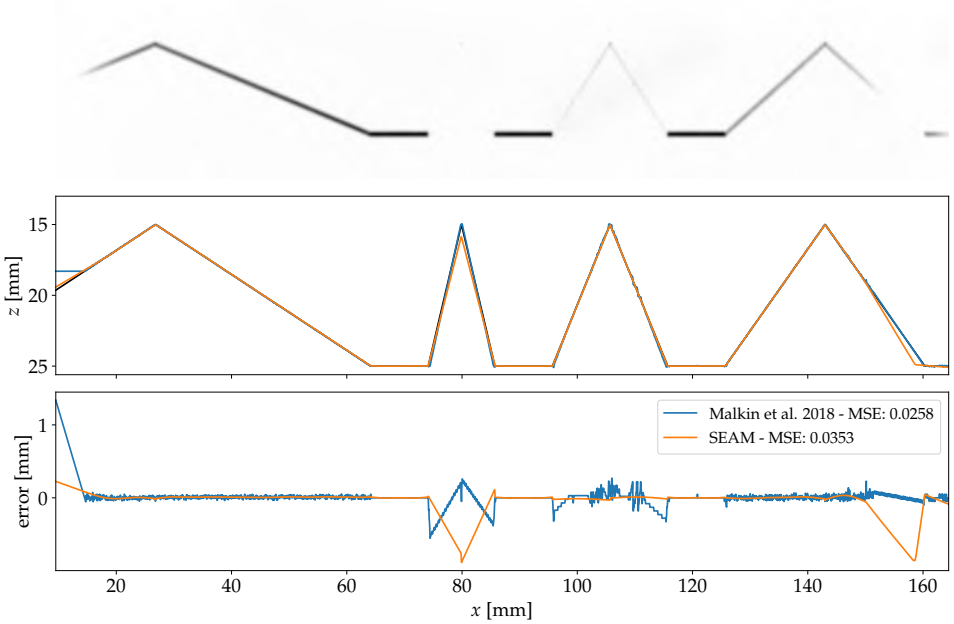

Source: Own authorship.

Figure 28 – A zoomed in view reveals the smoothness of the SEAM estimate against the reference method.

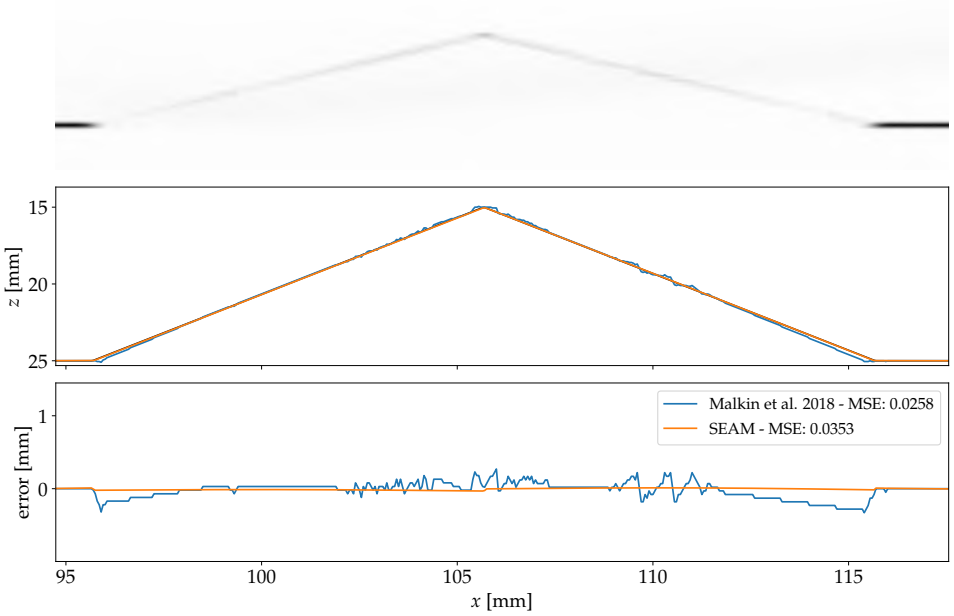

Source: Own authorship.

This same scenario was run with an SNR of 25 dB. The results, presented in Figure 29, show that SEAM removes some of the noise. The result can be improved by increasing τ in order to reduce the noise in the estimate and obtain a higher fidelity. Still, SEAM presented an MSE much lower than Malkin's method. In Figure 29 it is noticeable that near the border of the image, the reconstruction failed to approximate the reference line.

Figure 29 – Surface estimation in a simulated scenario with an SNR level of 25 dB. The MSE for both methods was greatly increased, still, SEAM performed much better than Malkin's method.

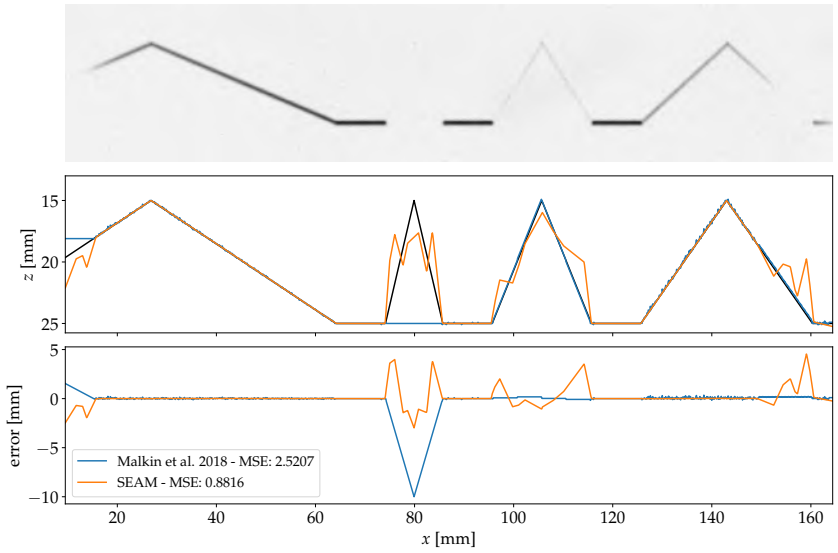

Source: Own authorship.

Another test was performed on a set of 10 acrylic specimens with curved surfaces. These specimens were described in (MALKIN *et al.*, 2018), as a way to evaluate surfaces with different gradients. An example of such specimen is shown in Figure 30. These specimens have 10 regions with the shape of sine wave, with each region having a length of one wavelength, ψ_n. Also, each specimen have a distinct amplitude for every region, denoted as A_m. These parameters are used to create a wide range of surface gradients, over which the methods are evaluated. If the maximum surface gradient in a given region is high, the image for this region will present low intensity as seen in Figure 30. Table 8 summarizes the dimensions of the specimens.

Table 8 – Values for ψ_n and A_m used in the design of the ten specimens. The values of m indicate the specimen while the values of n refer to regions on each specimen. For reference, the wavelength in water is approximately 0.3 mm.

n	1	2	3	4	5	6	7	8	9	10
ψ_n (mm)	108.12	67.58	54.06	21.62	10.81	6.76	5.41	4.32	3.60	2.70
m	1	2	3	4	5	6	7	8	9	10
A_m (mm)	2.00	5.11	8.22	11.33	14.44	17.56	20.67	23.78	26.89	30.00

Source: Own authorship.

The accuracy of both surface estimation methods were compared using three different criteria: overall MSE for each specimen and, mean and maximum errors in each of the 100 regions. By being a single value metric, MSE is a simpler way to compare the performance of the methods. Table 9 shows the MSE values obtained. With the exception of specimens 4 and 5, SEAM presented lower MSE, that is, found a more accurate estimate of the surface profile.

Table 9 – Comparison of MSE between SEAM and the method by Malkin *et al.* (2018). The MSE for both methods is very similar for the first two specimens, but, up to a point, the differences increase with A_m.

m	A_m (mm)	MSE		Improvement
		Malkin et al. 2018	SEAM	
1	2.00	0.025	0.005	0.020
2	5.11	0.091	0.028	0.063
3	8.22	0.175	0.175	0.000
4	11.33	0.285	0.391	-0.106
5	14.44	0.387	1.450	-1.063
6	17.56	1.753	1.332	0.421
7	20.67	4.650	3.522	1.128
8	23.78	6.393	5.275	1.118
9	26.89	12.858	9.752	3.106
10	30.00	23.551	16.418	7.133

Source: Own authorship.

Looking at each region individually brings more information on the weaknesses of each method. When comparing the methods by their performances on single regions, it gets harder to define a winner. Figure 31 illustrates the differences of performance by both methods.

Figure 30 – Prototype specimen (a) used in the surface estimation experiment of curved specimens. Parameter A_m varies between specimens and ψ_n varies within specimens. Parameter A_m affects the maximum gradient in each region. Higher gradient regions are hard to image than lower gradient regions, as shown in (b) and (c).

(a) Prototype specimen

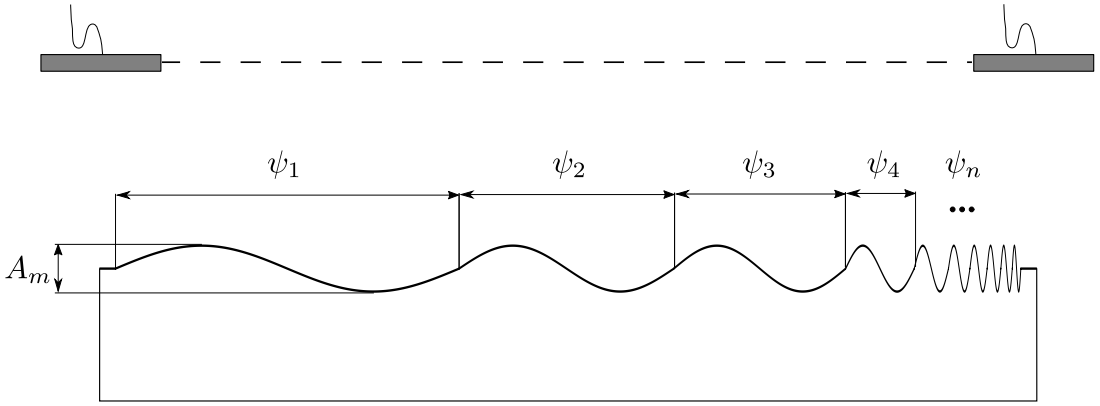

(b) Specimen A_1

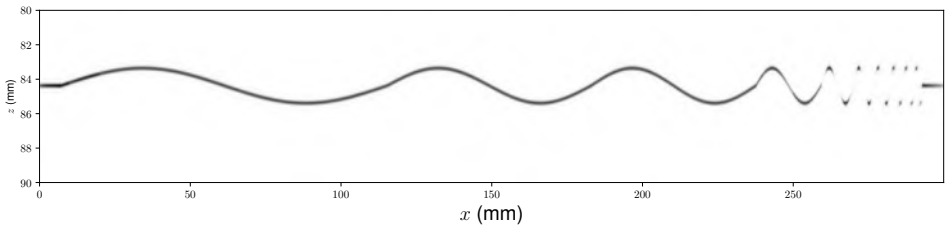

(c) Specimen A_{10}

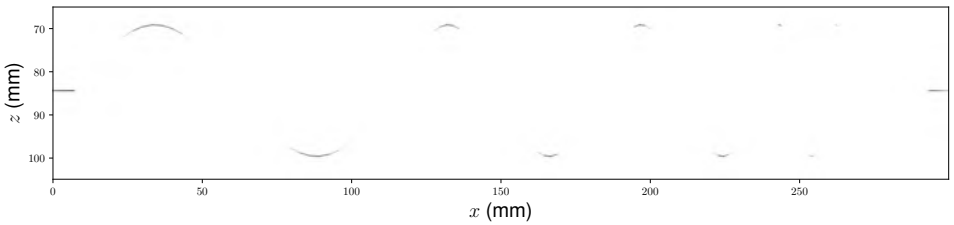

Source: Own authorship.

Each position on the image shows the error, mean or maximum, on the given region of a given specimen. That is, position (m, n) is the error obtained in region ψ_n of specimen A_m. The magnitude of the error is encoded by the color.

When looking at the mean errors, SEAM presents the single higher mean error for $A_m = 8$ and $\psi_n = 10$, but overall, it presents lower error than the reference method. When looking at maximum errors, both methods are pretty close but SEAM presents more errors for higher ψ_n even with lower amplitude. Close analysis of these images show that the MSE for each specimen,

showed in Table 9, is dominated by the errors in higher ψ_n regions. This means that for those regions, interior imaging is much harder than it is for regions of lower ψ_n, if possible at all.

Figure 31 – Comparison of mean and maximum errors, per region, between methods. Although harder to determine which method has better performance, this comparison highlights situations where the methods fail. The regions contourned in red present errors bigger than 1, in these regions imaging is expected to fail.

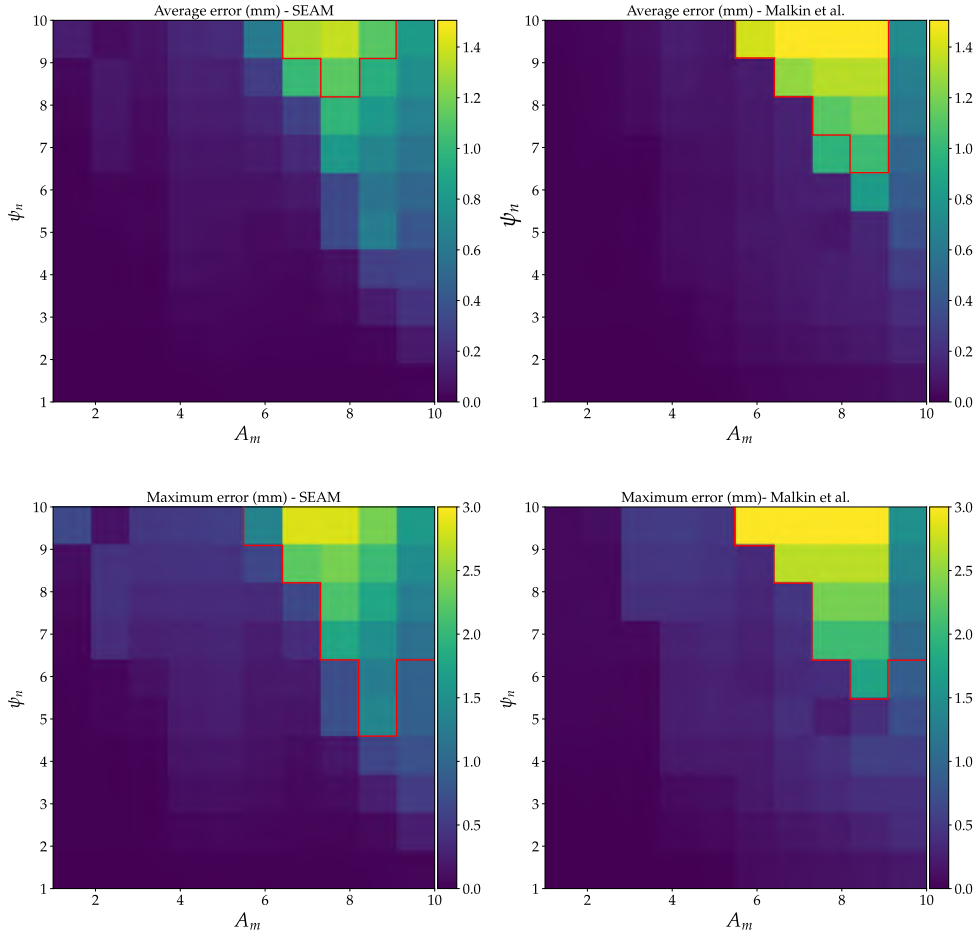

Source: Own authorship.

In the next section, both methods will be used to estimate surfaces from real data and these surfaces will be used to produce interior images of the inspected objects.

4.4 EXPERIMENTS

Experiments were carried out using an M2M Panther^{TM} (Eddyfi NDT, Inc.) Acquisition System and a 64-elements linear array from Imasonic (IMASONIC SAS, France). Relevant information about the array is summarized in Table 10. Again, the method presented in Malkin *et al.* (2018) is used as baseline for the profile estimation and both estimates are compared to a reference profile.

Table 10 – Acquisition system and transducer array parameters.

Setup Parameter	Value
Sampling Frequency (MHz)	125
Number of elements	64
Element pitch (mm)	0.6
Element width (mm)	0.5
Element length (mm)	10
Central Frequency (MHz)	5.2
Bandwidth at -6dB	71%

Source: Own authorship.

The fADMM algorithm, described in Algorithm 2, requires the definition of four additional parameters: τ, ρ, η and ϵ. The parameter η is set to 0.999, as recommended in (GOLDSTEIN *et al.*, 2014), while parameters ρ and ϵ are set to 100 and 10^{-6}, respectively. These values are kept for all experiments. Only parameter τ changes for each experiment, values in the range $[1, 80]$ were evaluated in order to obtain the best results in terms of MSE.

4.4.1 Experiment I

The first test aimed to estimate the bottom surface profile of the acrylic specimen shown in Figure 32, this specimen has the same dimensions as the one in Figure 26. This test emulates a corrosion mapping scenario. The array was moved in order to scan the specimen at 32 positions, starting with its center at 20 mm from the left corner and moving towards the right corner with uniform steps of 5 mm. At each position, an image was formed using TFM and all images were stitched together to form a single image of the bottom surface, as described in Section 2.5.

For this experiment, parameter τ was set to 2, according to the minimum in Figure 33. Figure 34 shows the TFM image along with the reference and estimated profiles. In the TFM image, it is noticeable that the sides of the narrowest triangle are indistinguishable and only the tip can be seen. Its sides are well approximated by the both estimates, which is expected since the reference is a straight line from the base to the tip.

Both methods presented low error when compared to the reference, but SEAM presented slightly lower MSE, a difference of 5.8×10^{-3}, or 15%. This difference reflects the smoothing effect of noise, specially in the peaks. As the real bottom surface is essentially composed of straight lines, both methods are well suited.

Figure 32 – Schematic of the acrylic specimen inspected and the probe's trajectory. The scanning starts with the UA centered at $x = 20$ mm and ends at $x = 180$ mm with steps of 5 mm. At each position an acquisition is done.

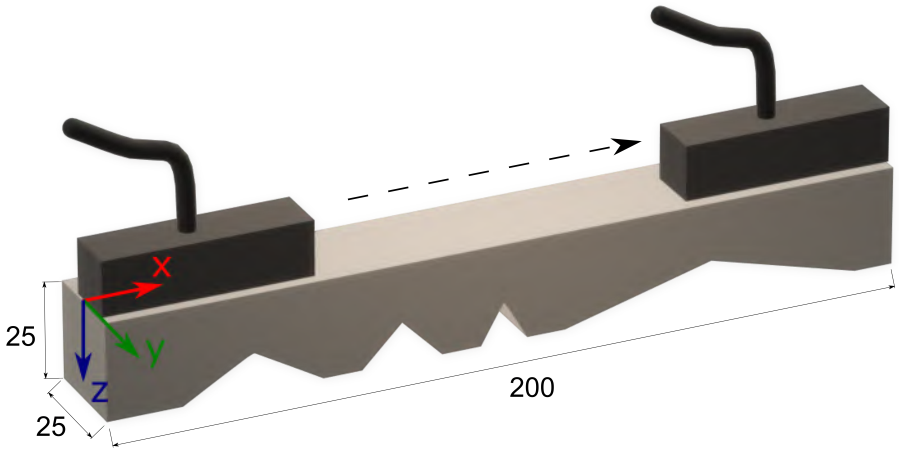

Source: Own authorship.

Figure 33 – Plot of MSE versus τ, ranging from 1 to 80. Best MSE was found using τ=2.

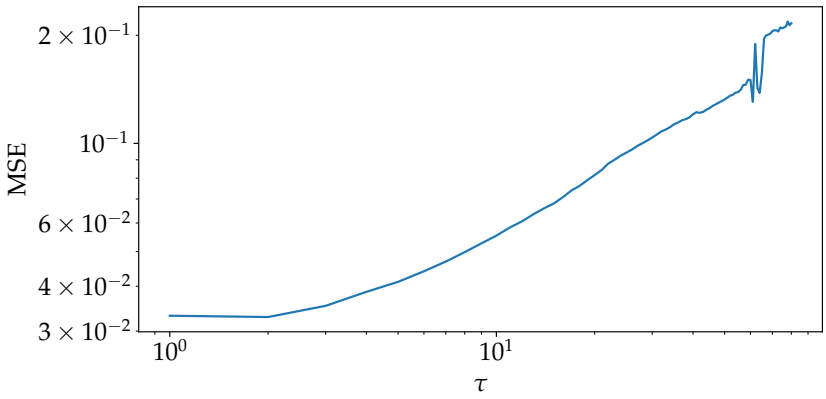

Source: Own authorship.

4.4.2 Experiment II

A second experiment was done using an acrylic specimen with a non-flat entry surface and two side drilled holes (SDH). The specimen, illustrated in Figure 35, was immersed in a water tank. The array was positioned 32 mm above the peaks of the specimen and 10 acquisitions were performed with the same 5 mm step. As the surface is wavy, the imposition of straight lines on the entry surface profile would lead to large errors. Given that, it is expected that the difference in MSE between the two tested methods increases.

For this experiment, the parameter τ for SEAM was set to 7, according to the minimum found in Figure 36. The reconstructed image and the estimated profiles are shown in Figure 37.

Figure 34 – TFM image of the bottom surface of an acrylic specimen and the profile estimates using two different surface extraction methods. Both show good agreement with the reference.

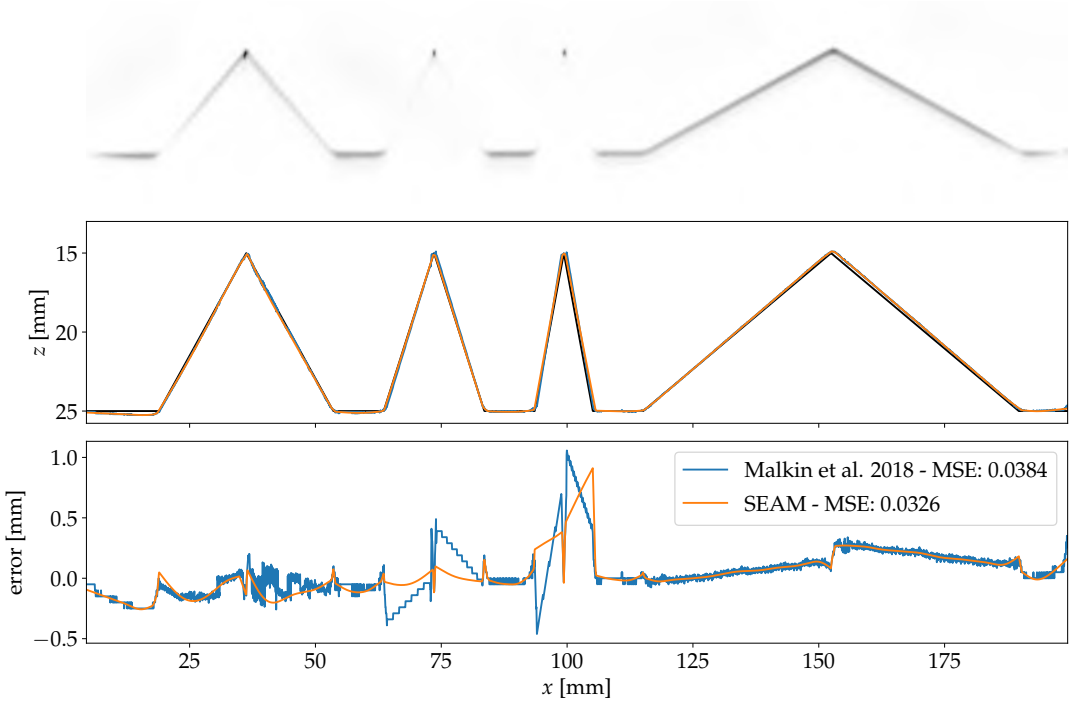

Source: Own authorship.

As the image presents an overall good Signal to Noise Ratio (SNR), both estimates presented low errors. SEAM obtained a smaller MSE, around 68%, a difference of 0.0137 when compared to the reference method.

Even though, in a section of the surface, showed in the left side of Figure 37, the amplitudes were too low and the reference method interpolated the missing points with a straight line. This led to a higher MSE than that obtained by our method. As expected, SEAM was capable of recovering the low amplitude points with higher accuracy in regions with lower SNR.

The interior imaging was performed once for each estimate, imaging the region with two SDHs. The results are compared in Figure 38. Although the estimates presented similar MSEs, the reconstructed images have a clearer difference. The image obtained using SEAM presents higher amplitude for the SDHs, making them more distinguishable. This is due to the smoother surface obtained by SEAM.

As the SDHs are not symmetrical with respect to the closest peak of the surface, the SDH on the right being closer to the peak, the intensities of the image are not identical.

Figure 35 – Specimen with a sine-like top surface with two SDHs. The specimen was fabricated in acrylic with sound speed of 2830 m/s. Dimensions are in millimeters.

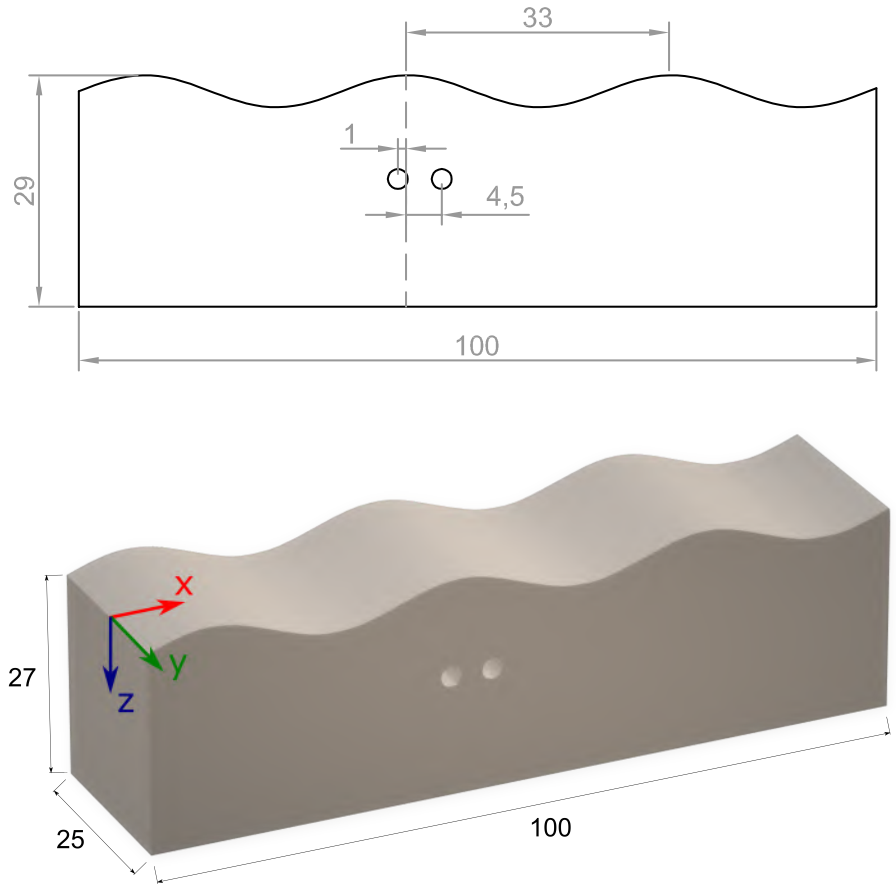

Source: Own authorship.

Figure 36 – Plot of MSE versus τ, ranging from 1 to 80. Best MSE was found using τ=7.

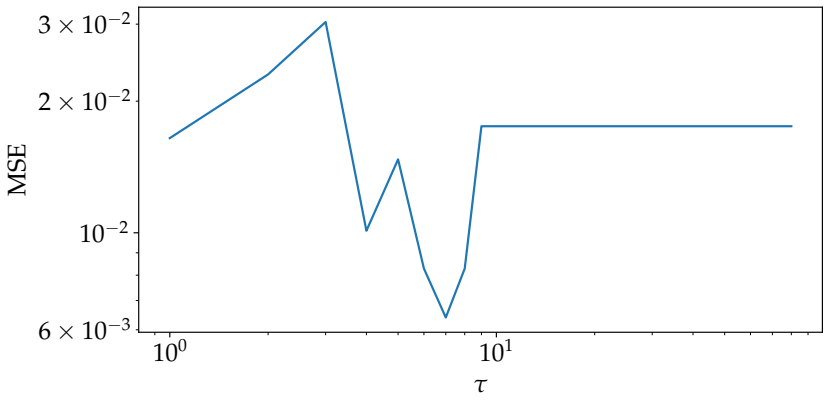

Source: Own authorship.

Figure 37 – TFM image of the top surface of the acrylic specimen and the estimates using two different surface extraction methods. Both method present good agreement with the reference in regions where the image presents high reflection values. Even in a low-amplitude region, SEAM was still capable of accurately estimating the surface.

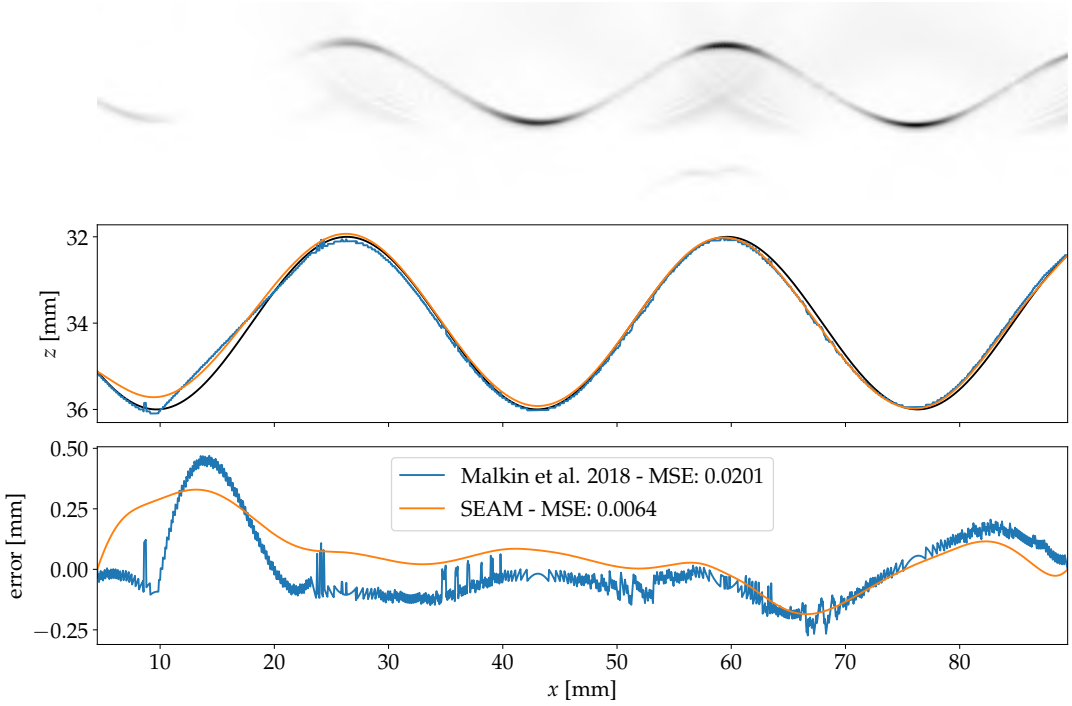

Source: Own authorship.

Figure 38 – Image of the both SDHs region using the surface profile estimates. The SDHs, denotted by the red circles, are more evident using SEAM.

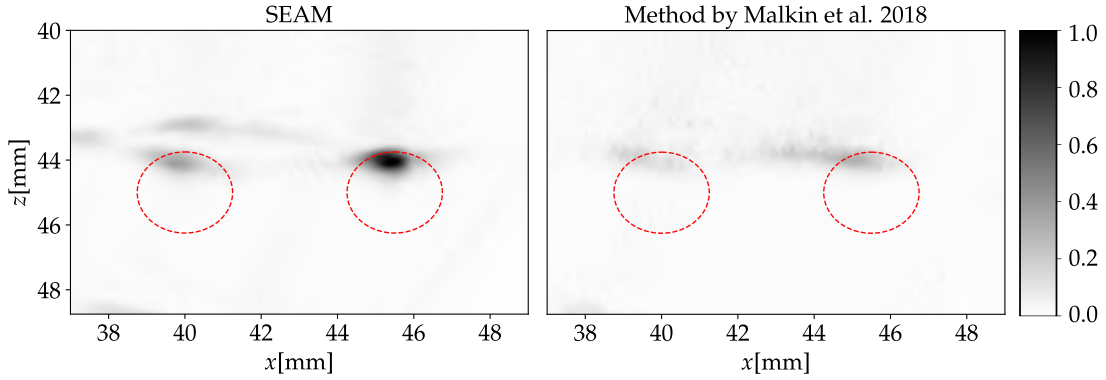

Source: Own authorship.

Figure 39 – Specimen with a concave top surface with two SDHs. The specimen was fabricated in acrylic with sound speed of 2830 m/s. Dimensions are in millimeters.

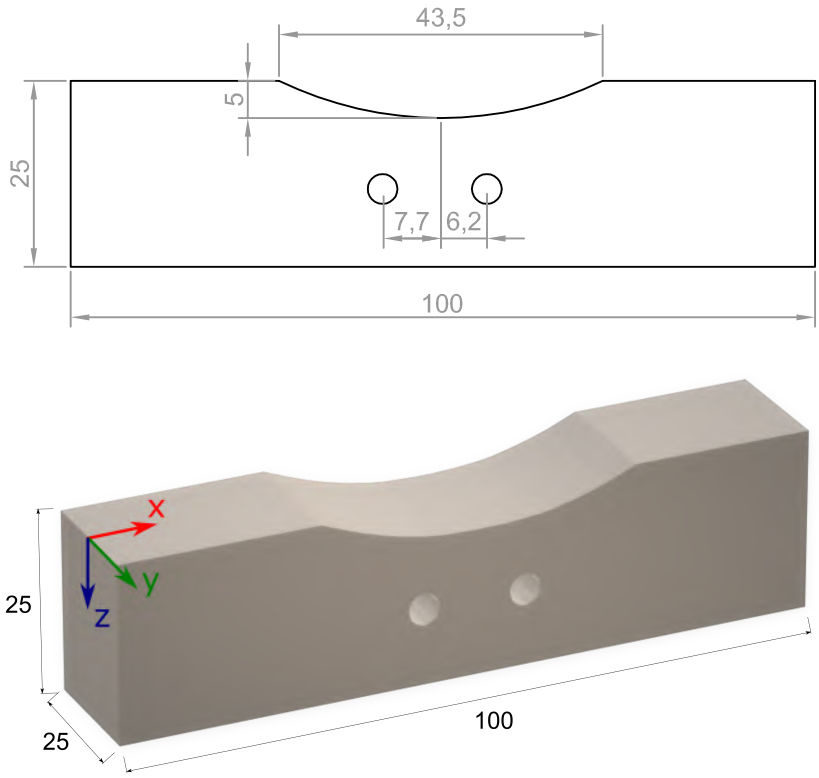

Source: Own authorship.

Figure 40 – Plot of MSE versus τ, ranging from 1 to 80. Best MSE was found using τ=44.

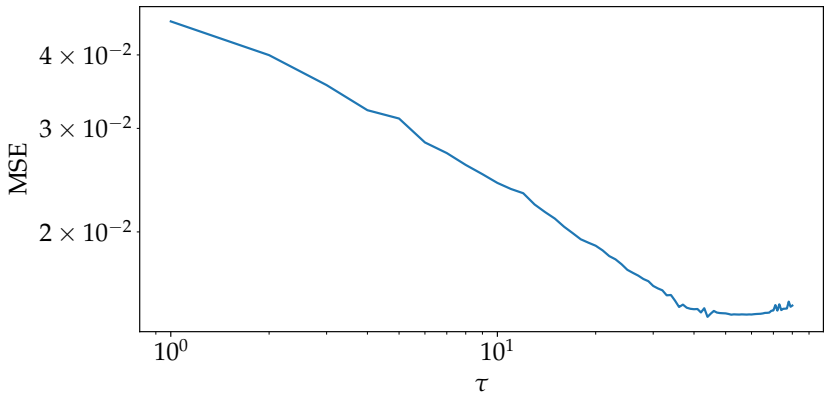

Source: Own authorship.

4.4.3 Experiment III

A third experiment was performed using an acrylic specimen with a convex region, as shown in Figure 39. As before, the specimen was immersed in a water tank and scanned in 10 positions 5 mm apart.

Figure 41 – TFM image of the top surface of an concave acrylic specimen and the estimates using two different surface extraction methods. The difference between the estimates is increased compared to previous comparisons.

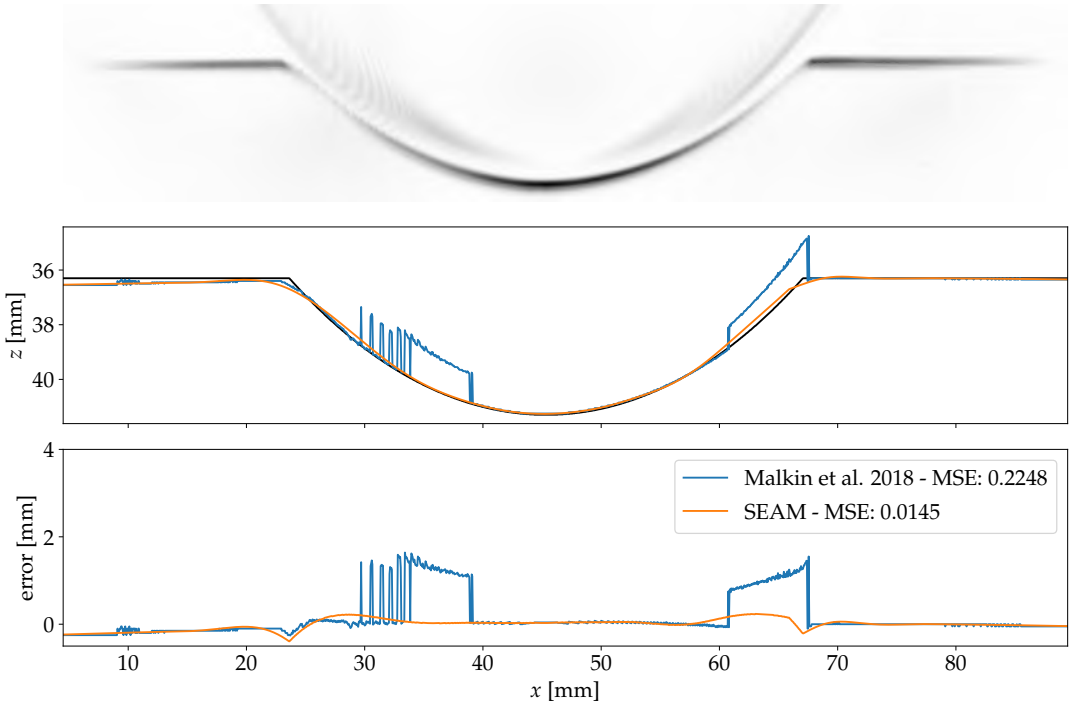

Source: Own authorship.

This experiment used $\tau = 44$ that was obtained by taking the minimum MSE in Figure 40. The TFM image and surface estimates are shown in Figure 41. Again, SEAM presented a better estimate, a difference of 0.2103 in MSE, aroun 94% smaller. The large difference in the performances of the two methods is due mainly to the fact that imaging artifacts were wrongly detected as entry surface in the method of Malkin *et al.* (2018).

Figure 42 shows a comparison between the interior images formed using both surface profiles. Using the surface estimated by SEAM, both SDHs are clearly visible. Using the reference method resulted in lower amplitudes and the left SDH being barely visible. It is important to note, these SDHs are not symmetrical, in relation to the center of the specimen, so their intensities would not be identical.

The results of these experiments are summarized in Table 11. These experiments show that SEAM is capable of surpassing the reference method in some scenarios. Also, it is shown that the more accurate estimated profiles led to better interior imaging of the inspected specimens.

Figure 42 – Image of the both SDHs region using the surface profile estimates. The SDHs are denotted by the red circles. Again, the surface obtained with SEAM lead to better visualization of the SDHs.

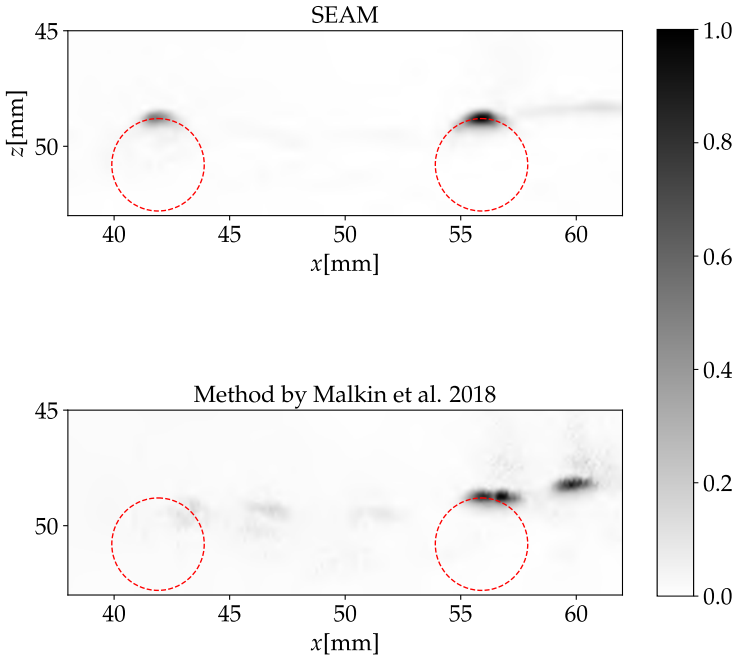

Source: Own authorship.

Table 11 – Comparison of estimated profiles MSE. In each experiment SEAM, SEAM, presented better MSE than the reference method (MALKIN *et al.*, 2018).

MSE	Reference Method	SEAM
Experiment I	0.0384	0.0326
Experiment II	0.0201	0.0064
Experiment III	0.2248	0.0145

Source: Own authorship.

4.5 COMMENTARIES

An inverse problem formulation was proposed in order to improve surface profile estimation. This formulation includes a second-order TV regularization term to promote piecewise linear solutions. Also, it takes into account the different SNR levels across observations by including a weighting matrix in the data fidelity term. It was shown that this new method is more robust to noise than the state-of-the-art method (MALKIN *et al.*, 2018) for 1D surface profile estimation.

The contributions of this study are: (1) probabilistic modelling of the estimator $\check{\mathbf{z}}$ error and (2) a method for surface estimation that is robust to noise. Still, a more theoretical approach to the choice of parameter λ is desired.

The next steps of this study are: (1) reevaluate the existence of correlation between observations; (2) develop robust procedures for the choice of τ; (3) generalize the method for 2D surfaces.

5 FINAL REMARKS

Ultrasound imaging is a handy resource for NDT due to its low cost, portability and safety. With array probes becoming feasible and cheaper, methods based on post-processing beamforming, such as the TFM, became the golden standard. Such methods rely on prior knowledge of inspection parameters in order to calculate wave trajectories and produce focused images. These parameters include the sound speed in the inspected materials and the shape of inspection objects, among others.

This study was focused on the development of experimental procedures for the estimation of the these parameters. Methods to estimate sound speed in inspected materials were discussed in Chapter 3. These methods are capable of producing good estimates with low uncertainty. Both methods are based on the same principle of image quality assessment, the difference being the optimization method. The first method finds the optimal speed using a grid search. This method was reported in (MOURA *et al.*, 2019; MOURA *et al.*, 2020).

The second method uses an optimization scheme called Brent's method, which is a combination of Golden Section Search with parabolic interpolation steps that accelerates convergence. It was verified that this method converges to a solution faster than the grid search, but with an increased uncertainty. This method was also tested in a simulated scenario with images containing only a speckle pattern. Even in this scenario the method was able to produce estimates with low bias.

In Chapter 4, a method for estimating an objects surface was proposed. The method takes as input a B-scan image, created with a method such as the TFM, and makes an initial estimate of the surface profile. This initial estimate is then refined by solving a constrained inverse problem. The inverse problem formulation consists of a WLS term and a second-order TV regularization term. This formulation promotes solutions that are piecewise linear in regions with low SNR. In regions with higher SNR, the estimate is closer to the initial estimate but, possibly, less noisy. The relation of the SNR to the weights in WLS is analyzed in Appendix A.

This method was developed for 1D surface profiles but can be extended to work with 2D surfaces. Another viable extension is a regularization term with third-order total variation that promotes piecewise smooth surfaces as solutions.

Future works in the sound speed estimation theme include:

- Automation of the surface masking process for immersion testing;
- Development of a learned metric for images;
- Development of a reference-free method for direction-dependent sound speed estimation.

For the surface reconstruction theme, future works include:

- Reevaluation of the existence of correlation between observed points;
- Development of robust procedures for the choice of τ;
- Generalization of the 1D surface profile estimation to 2D surfaces.

REFERENCES

ABD-ELMONIEM, K.Z.; KADAH, Y.M.; YOUSSEF, A.-B.M. Real time adaptive ultrasound speckle reduction and coherence enhancement. *In*: **Proceedings 2000 International Conference on Image Processing (Cat. No.00CH37101)**. *[S.l.: s.n.]*, 2000. v. 1, p. 172–175 vol.1. ISSN: 1522-4880.

ABE, K.; ARAKAWA, M.; KANAI, H. Estimation method for sound velocity distribution for high-resolution ultrasonic tomographic imaging. **Journal of Medical Ultrasonics**, v. 46, n. 1, p. 27–33, 2019.

ADLER, L.; LEWIS, D. K. Scattering of a broadband ultrasonic pulse by discontinuities. **IEEE Transactions on Sonics Ultrasonics**, v. 23, p. 351–356, Sep. 1976.

ANDERSON, M. E.; MCKEAG, M. S.; TRAHEY, G. E. The impact of sound speed errors on medical ultrasound imaging. **The Journal of the Acoustical Society of America**, v. 107, n. 6, p. 3540–3548, May 2000. ISSN 0001-4966.

BEVAN, R. L. T.; ZHANG, J.; BUDYN, N.; CROXFORD, A. J.; WILCOX, P. D. Experimental Quantification of Noise in Linear Ultrasonic Imaging. **IEEE Transactions on Ultrasonics, Ferroelectrics, and Frequency Control**, v. 66, n. 1, p. 79–90, Jan. 2019. ISSN 1525-8955.

BORLOO, E. E. An ultrasonic technique for the inspection of magnetic and explosive welds, using a facsimile recording system. **Non-Destructive Testing**, v. 6, n. 1, p. 25–28, Feb. 1973. ISSN 0029-1021.

BRENT, R. P. Algorithms for Minimization Without Derivatives. **Dover Publications**, 2013. OCLC: 868274093.

BROWN, M.; LOWE, D. G. Automatic panoramic image stitching using invariant features. **International journal of computer vision**, Springer, v. 74, n. 1, p. 59–73, 2007.

CAMACHO, J.; CRUZA, J. F.; BRIZUELA, J.; FRITSCH, C. Automatic dynamic depth focusing for NDT. **IEEE Transactions on Ultrasonics, Ferroelectrics, and Frequency Control**, v. 61, n. 4, p. 673–684, Apr. 2014. ISSN 1525-8955.

CARVALHO, A. A.; REBELLO, J. M. A.; SOUZA, M. P. V.; SAGRILO, L. V. S.; SOARES, S. D. Reliability of non-destructive test techniques in the inspection of pipelines used in the oil industry. **International journal of pressure vessels and piping**, Elsevier, v. 85, n. 11, p. 745–751, 2008.

CHAMBOLLE, A. Total Variation Minimization and a Class of Binary MRF Models. *In*: **Energy Minimization Methods in Computer Vision and Pattern Recognition**. *[S.l.]*: Springer, Berlin, Heidelberg, 2005. p. 136–152.

CHAN, T.F.; OSHER, S.; SHEN, J. The digital TV filter and nonlinear denoising. **IEEE Transactions on Image Processing**, v. 10, n. 2, p. 231–241, Feb. 2001. ISSN 1941-0042.

CHAN, T. F.; MARQUINA, A.; MULET, P. High-Order Total Variation-Based Image Restoration. **SIAM Journal on Scientific Computing**, v. 22, n. 2, p. 503–516, Jan. 2000. ISSN 1064-8275.

CIVA in a few words. 2021. Available at: https://www.extende.com/civa-in-a-few-words.

DIARRA, B.; LIEBGOTT, H.; TORTOLI, P.; CACHARD, C. Sparse array techniques for 2D array ultrasound imaging. *In*: D'ACOUSTIQUE, Société Française (Ed.). **Acoustics 2012**. Nantes, France: *[s.n.]*, 2012.

DIARRA, B.; ROBINI, M.; TORTOLI, P.; CACHARD, C.; LIEBGOTT, H. Design of Optimal 2-D Nongrid Sparse Arrays for Medical Ultrasound. **IEEE Transactions on Biomedical Engineering**, v. 60, n. 11, p. 3093–3102, Nov. 2013. ISSN 1558-2531.

DIXON, S.; BURROWS, S. E.; DUTTON, B.; FAN, Y. Detection of cracks in metal sheets using pulsed laser generated ultrasound and EMAT detection. **Ultrasonics**, v. 51, n. 1, p. 7–16, Jan. 2011. ISSN 0041-624X.

DIXON, S.; EDWARDS, C.; PALMER, S. B. A laser–EMAT system for ultrasonic weld inspection. **Ultrasonics**, v. 37, n. 4, p. 273–281, Apr. 1999. ISSN 0041-624X.

DOCTOR, S. R.; HALL, T. E.; REID, L. D. SAFT — the evolution of a signal processing technology for ultrasonic testing. **NDT International**, v. 19, n. 3, p. 163–167, Jun. 1986. ISSN 0308-9126.

DUXBURY, A. C. Seawater. **Encyclopedia Britannica**, Nov. 2020. Available at: https://www.britannica.com/science/seawater.

D.V.M, Z. W.; SIMONCELLI, E. P. Reduced-reference image quality assessment using a wavelet-domain natural image statistic model. *In*: **Human Vision and Electronic Imaging X**. *[S.l.]*: International Society for Optics and Photonics, 2005. v. 5666, p. 149–159.

ELAD, M.; MILANFAR, P.; RUBINSTEIN, R. Analysis versus synthesis in signal priors. **Inverse Problems**, v. 23, n. 3, p. 947–968, Apr. 2007. ISSN 0266-5611.

EVERTON, S. K.; HIRSCH, M.; STRAVROULAKIS, P.; LEACH, R. K.; CLARE, A. T. Review of in-situ process monitoring and in-situ metrology for metal additive manufacturing. **Materials & Design**, Elsevier, v. 95, p. 431–445, 2016.

GIURGIUTIU, V.; CUC, A. Embedded non-destructive evaluation for structural health monitoring, damage detection, and failure prevention. **Shock and Vibration Digest**, Citeseer, v. 37, n. 2, p. 83, 2005.

GOLDSTEIN, T.; O'DONOGHUE, B.; SETZER, S.; BARANIUK, R. G. Fast Alternating Direction Optimization Methods. **SIAM J. Imaging Sciences**, 2014.

HARPUT, S.; CHRISTENSEN-JEFFRIES, K.; RAMALLI, A.; BROWN, J.; ZHU, J.; ZHANG, G.; LEOW, C. H.; TOULEMONDE, M.; BONI, E.; TORTOLI, P.; ECKERSLEY, R. J.; DUNSBY, C.; TANG, M.-X. 3-D Super-Resolution Ultrasound Imaging With a 2-D Sparse Array. **IEEE Transactions on Ultrasonics, Ferroelectrics, and Frequency Control**, v. 67, n. 2, p. 269–277, Feb. 2020. ISSN 1525-8955.

HE, J.; ZHOU, R.; HONG, Z. Modified fast climbing search auto-focus algorithm with adaptive step size searching technique for digital camera. **IEEE Transactions on Consumer Electronics**, v. 49, n. 2, p. 257–262, May 2003.

HELLIER, C. Handbook of nondestructive evaluation, 3e. **McGraw-Hill Education**, 2020.

HOLMES, C.; DRINKWATER, B.; WILCOX, P. The post-processing of ultrasonic array data using the total focusing method. **The British Institute of Non-Destructive Testing**, Nov. 2004.

HOLMES, C.; DRINKWATER, B. W.; WILCOX, P. D. Post-processing of the full matrix of ultrasonic transmit–receive array data for non-destructive evaluation. **NDT & E International**, v. 38, n. 8, p. 701–711, Dec. 2005. ISSN 0963-8695.

HSU, DK. Non-destructive evaluation (nde) of aerospace composites: ultrasonic techniques. *In*: **Non-destructive evaluation (NDE) of polymer matrix composites**. *[S.l.]*: Elsevier, 2013. p. 397–422.

HUNTER, A. J.; DRINKWATER, B. W.; WILCOX, P. D. The wavenumber algorithm for full-matrix imaging using an ultrasonic array. **IEEE Transactions on Ultrasonics, Ferroelectrics, and Frequency Control**, v. 55, n. 11, p. 2450–2462, Nov. 2008. ISSN 0885-3010.

HUNTER, A. J.; DRINKWATER, B. W.; WILCOX, P. D. Autofocusing ultrasonic imagery for non-destructive testing and evaluation of specimens with complicated geometries. **NDT & E International**, v. 43, n. 2, p. 78–85, Mar. 2010. ISSN 0963-8695.

HUNTER, A. J.; DRINKWATER, B. W.; WILCOX, P. D. A model-based autofocus algorithm for ultrasonic imaging using a flexible array. **AIP Conference Proceedings**, v. 1211, n. 1, p. 863–870, Feb. 2010. ISSN 0094-243X.

HUNTER, A. J.; DRINKWATER, B. W.; WILCOX, P. D. Least-squares estimation of imaging parameters for an ultrasonic array using known geometric image features. **IEEE Transactions on Ultrasonics, Ferroelectrics, and Frequency Control**, v. 58, n. 2, p. 414–426, Feb. 2011.

HWANG, J. S.; SHIN, H. J.; SONG, S. J.; SONG, T. K. Digital Phased Array Ultrasonic Inspection system with dynamic focusing. **AIP Conference Proceedings**, v. 509, n. 1, p. 1087–1094, May 2000. ISSN 0094-243X.

JAKOVLJEVIC, M.; HSIEH, S.; ALI, R.; KUNG, G. Chau Loo; HYUN, D.; DAHL, J. J. Local speed of sound estimation in tissue using pulse-echo ultrasound: Model-based approach. **The Journal of the Acoustical Society of America**, v. 144, n. 1, p. 254–266, Jul. 2018. ISSN 0001-4966.

JCGM. JCGM 100:2008 - Evaluation of measurement data — Guide to the expression of uncertainty in measurement. **JCGM 2008**, 2008.

KINO, G. S. Acoustic imaging for nondestructive evaluation. **Proceedings of the IEEE**, v. 67, n. 4, p. 510–525, Apr. 1979. ISSN 1558-2256.

KO, Y.; LEE, J.; JUNG, Y.; KIM, B.; KO, S. An advanced camera system having fast autofocus control. *In*: **ICCE. International Conference on Consumer Electronics (IEEE Cat. No.01CH37182)**. *[S.l.: s.n.]*, 2001. p. 210–211.

KRAUT, E. A. Review of Theories of Scattering of Elastic Waves by Cracks. **IEEE Transactions on Sonics and Ultrasonics**, v. 23, n. 3, p. 162–167, May 1976. ISSN 2162-1403.

LE JEUNE, L., L.; ROBERT, S.; DUMAS, P.; MEMBRE, A.; PRADA, C. Adaptive ultrasonic imaging with the total focusing method for inspection of complex components immersed in water. **AIP Conference Proceedings**, v. 1650, n. 1, p. 1037–1046, Mar. 2015. ISSN 0094-243X.

LE JEUNE, L., L.; ROBERT, S.; PRADA, C. Plane wave imaging for ultrasonic inspection of irregular structures with high frame rates. **AIP Conference Proceedings**, v. 1706, n. 1, p. 020010, Feb. 2016. ISSN 0094-243X.

LE JEUNE, L., L.; ROBERT, S.; VILLAVERDE, E. L.; PRADA, C. Plane Wave Imaging for ultrasonic non-destructive testing: Generalization to multimodal imaging. **Ultrasonics**, v. 64, p. 128–138, 2016.

LE, T.; GIBB, S.; PHAM, N.; LA, H. M.; FALK, L.; BERENDSEN, T. Autonomous robotic system using non-destructive evaluation methods for bridge deck inspection. *In*: IEEE. **2017 IEEE International Conference on Robotics and Automation (ICRA)**. *[S.l.]*, 2017. p. 3672–3677.

LEE, S.; KALOS, N. *et al.* Non-destructive testing methods in the us for bridge inspection and maintenance. **KSCE Journal of Civil Engineering**, Springer, v. 18, n. 5, p. 1322–1331, 2014.

LI, Y.; NEWHOUSE, V. L.; SHANKAR, P. M.; KARPUR, P. Speckle reduction in ultrasonic synthetic aperture images. **Ultrasonics**, v. 30, n. 4, p. 233–237, Jan. 1992. ISSN 0041-624X.

LIANG, T.; YUNG, L.; YU, W. On Feature Motion Decorrelation in Ultrasound Speckle Tracking. **IEEE Transactions on Medical Imaging**, v. 32, n. 2, p. 435–448, Feb. 2013. ISSN 1558-254X.

LONG, R.; CAWLEY, P. Further development of a conformable phased array device for inspection over irregular surfaces. *In*: AMERICAN INSTITUTE OF PHYSICS. **AIP Conference Proceedings**. *[S.l.]*, 2008. v. 975, n. 1, p. 754–761.

MAIERHOFER, C. Nondestructive evaluation of concrete infrastructure with ground penetrating radar. **Journal of materials in civil engineering**, American Society of Civil Engineers, v. 15, n. 3, p. 287–297, 2003.

MALKIN, R. E.; FRANKLIN, A. C.; BEVAN, R. L. T.; KIKURA, H.; DRINKWATER, B. W. Surface reconstruction accuracy using ultrasonic arrays: Application to non-destructive testing. **NDT & E International**, v. 96, p. 26–34, Jun. 2018. ISSN 0963-8695.

MATERIAL Sound Velocities | Olympus IMS. 2021. Available at: https://www.olympus-ims.com/pt/ndt-tutorials/thickness-gauge/appendices-velocities/.

MCKEE, J. G.; BEVAN, R. L. T.; WILCOX, P. D.; MALKIN, R. E. Volumetric imaging through a doubly-curved surface using a 2D phased array. **NDT & E International**, v. 113, p. 102260, Jul. 2020. ISSN 0963-8695.

MILLON, C.; VANHOYE, A.; OBATON, A.; PENOT, J. Development of laser ultrasonics inspection for online monitoring of additive manufacturing. **Welding in the World**, Springer, v. 62, n. 3, p. 653–661, 2018.

MONTALDO, G.; TANTER, M.; BERCOFF, J.; BENECH, N.; FINK, M. Coherent plane-wave compounding for very high frame rate ultrasonography and transient elastography. **IEEE Transactions on Ultrasonics, Ferroelectrics, and Frequency Control**, v. 56, n. 3, p. 489–506, Mar. 2009.

MOURA, H. L.; SILVA, V. O.; GUARNERI, G. A.; GUERREIRO, M. T. L.; PASSARIN, T. A. R.; PIRES, G. P.; PIPA, D. R. Image-Based Ultrasound Speed Estimation in Isotropic Materials. **IEEE Sensors Journal**, p. 1–1, 2020. ISSN 1558-1748.

MOURA, H. L. de; SILVA, V. O.; GUARNERI, G. A.; PASSARIN, T. A. R.; PIPA, D. R.; PIRES, G. P. Image-based ultrasound speed estimation for NDT in homogeneous media. **Review of Progress in Quantitative Nondestructive Evaluation**, Dec. 2019.

NAPOLITANO, D.; CHOU, C.; MCLAUGHLIN, G.; JI, T.; MO, L.; DEBUSSCHERE, D.; STEINS, R. Sound speed correction in ultrasound imaging. **Ultrasonics**, v. 44, p. e43–e46, Dec. 2006. ISSN 0041-624X.

NARAYANAN, S. K.; WAHIDABANU, R. S. D. A View on Despeckling in Ultrasound Imaging. **International Journal of Signal Processing, Image Processing and Pattern Recognition**, v. 2, n. 3, 2009.

NESTEROV, Y. E. A method for solving the convex programming problem with convergence rate O(1/k^2). **Dokl. Akad. Nauk SSSR**, v. 269, p. 543–547, 1983.

NOVA série de sondas para solda. 2021. Available at: https://www.olympus-ims.com/pt/probes/pa/weld-series/.

RIEDER, H.; DILLHÖFER, A.; SPIES, M.; BAMBERG, J.; HESS, T. Online monitoring of additive manufacturing processes using ultrasound. *In*: **ECNDT**. *[S.l.: s.n.]*, 2014. p. 6–10.

RIZZO, P.; MARZANI, A.; BRUCK, J. *et al.* Ultrasonic guided waves for nondestructive evaluation/structural health monitoring of trusses. **Measurement science and technology**, IOP Publishing, v. 21, n. 4, p. 045701, 2010.

RUDIN, L. I.; OSHER, S.; FATEMI, E. Nonlinear total variation based noise removal algorithms. **Physica D: Nonlinear Phenomena**, v. 60, n. 1, p. 259–268, Nov. 1992. ISSN 0167-2789.

RUSSELL, J.; LONG, R.; DUXBURY, D.; CAWLEY, P. Development and implementation of a membrane-coupled conformable array transducer for use in the nuclear industry. **The British Institute of Non-Destructive Testing**, Jul. 2012.

SCHMERR, L. W. Fundamentals of Ultrasonic Phased Arrays. **Springer International Publishing**, Aug. 2014. Google-Books-ID: py8goAEACAAJ.

SIMONETTI, F.; HUANG, L. From beamforming to diffraction tomography. **Journal of Applied Physics**, American Institute of Physics, v. 103, n. 10, p. 103110, 2008.

SONG, S.; SHIN, H. J.; JANG, Y. H. Development of an ultra sonic phased array system for nondestructive tests of nuclear power plant components. **Nuclear Engineering and Design**, v. 214, n. 1, p. 151–161, May 2002. ISSN 0029-5493.

STEPINSKI, T. An Implementation of Synthetic Aperture Focusing Technique in Frequency Domain. **IEEE Transactions on Ultrasonics, Ferroelectrics, and Frequency Control**, v. 54, n. 7, p. 1399–1408, Jul. 2007. ISSN 0885-3010.

STRUTZ, T. Data Fitting and Uncertainty: A practical introduction to weighted least squares and beyond. **Springer Vieweg**, 2016.

TREEBY, B. E.; VARSLOT, T. K.; ZHANG, E. Z.; LAUFER, J. G.; BEARD, P. C. Automatic sound speed selection in photoacoustic image reconstruction using an autofocus approach. **Journal of Biomedical Optics**, v. 16, n. 9, p. 090501, Sep. 2011. ISSN 1083-3668, 1560-2281.

TREMBLAY, Patrick; RICHARD, Daniel; ZETEC. Development and Validation of a Full Matrix Capture Solution. *In*: **9th International Conference on NDE in Relation to Structural Integrity for Nuclear and Pressurized Components**. *[S.l.: s.n.]*, 2013.

VIAL, J. Strong and weak convexity of sets and functions. **Mathematics of Operations Research**, INFORMS, v. 8, n. 2, p. 231–259, 1983.

WANG, Z. Applications of Objective Image Quality Assessment Methods [Applications Corner]. **IEEE Signal Processing Magazine**, v. 28, n. 6, p. 137–142, Nov. 2011. ISSN 1053-5888, 1558-0792.

WANG, Z.; BOVIK, A. C.; LU, L. Why is image quality assessment so difficult? *In*: **2002 IEEE International Conference on Acoustics, Speech, and Signal Processing**. *[S.l.: s.n.]*, 2002. v. 4, p. IV–3313–IV–3316. ISSN: 1520-6149.

WANG, Z.; SHEIKH, H.R.; BOVIK, A.C. No-reference perceptual quality assessment of JPEG compressed images. *In*: **Proceedings. International Conference on Image Processing**. *[S.l.: s.n.]*, 2002. v. 1, p. I–I. ISSN: 1522-4880.

WELLS, P. N. T.; HALLIWELL, M. Speckle in ultrasonic imaging. **Ultrasonics**, v. 19, n. 5, p. 225–229, Sep. 1981. ISSN 0041-624X.

WONG, G. S. K.; ZHU, S. Speed of sound in seawater as a function of salinity, temperature, and pressure. **The Journal of the Acoustical Society of America**, v. 97, n. 3, p. 1732–1736, Mar. 1995. ISSN 0001-4966.

ZHANG, J.; DRINKWATER, B. W.; WILCOX, P. D. Efficient immersion imaging of components with nonplanar surfaces. **IEEE Transactions on Ultrasonics, Ferroelectrics, and Frequency Control**, v. 61, n. 8, p. 1284–1295, Aug. 2014. ISSN 1525-8955.

APPENDIX

APPENDIX A – PROBABILITY OF ERROR IN PEAK ESTIMATION WITH RAYLEIGH DISTRIBUTED NOISE

The choice for $F(\cdot)$ in Chapter 4 should take into account the characteristics of $\mathbf{r} = \mathbf{z} - \check{\mathbf{x}}$. To analyze it, it is assumed that every position of $\mathbf{r}$ has the same characteristics. With this assumption, the analysis of a single position is enough.

First, a column of a TFM image is modeled as

$$s[z] = a.s^*[z] + n[z], \tag{22}$$

where

$$s^*[z] = \exp\left(-\frac{1}{2}\left(\frac{z - z^*}{b}\right)^2\right), \tag{23}$$

$a \in [0,1]$ is the amplitude of the echo in a given column, z^* is the position of the echo, b is related to the wavelength and n is the noise model. Bevan *et al.* (2019) recently demonstrated that noise in a TFM image can be modelled by a Rayleigh Distribution. So, it is considered that each position of n is independently and identically distributed from Rayleigh(σ). Figure 43 shown a comparison between a modeled column to a column from an image.

Figure 43 – Comparison of a column from a TFM image and the modeled column.

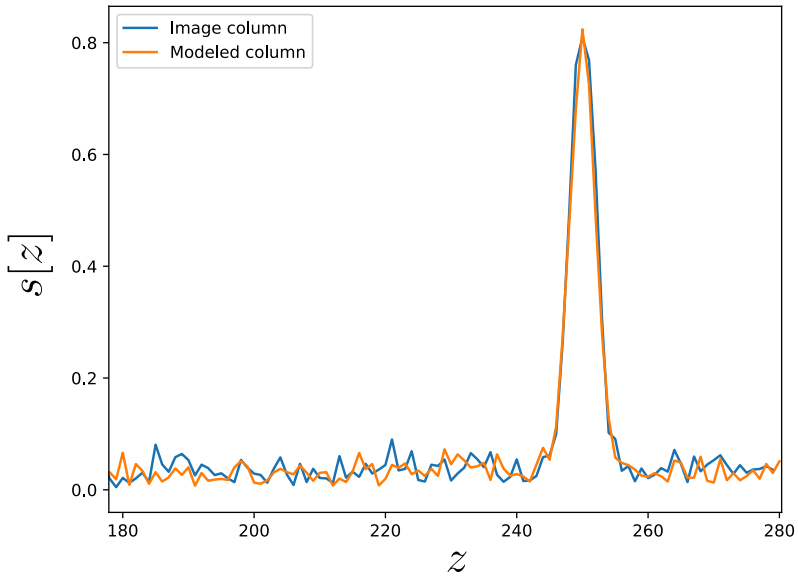

Source: Own authorship.

The estimator $\check{z}$ is obtained by finding the point that maximizes $s[z]$. Due to noise, the point of higher amplitude may not be the peak of $s^*[z]$. An error will occur whenever

$$s[z_k] > s[\check{z}], \tag{24}$$

that is

$$a.s^*[z_k] + n[z] > a.s^*[\check{z}] + n[\check{z}] \tag{25}$$

$$n[z_k] - n[\check{z}] > a.(s^*[\check{z}] - s^*[z]). \tag{26}$$

As the noise is i.i.d., the left side of the equation can be stated as

$$n[z] - n[\check{z}] = w[z] \sim p_w(z). \tag{27}$$

Substituting (27) in (26)

$$w[k] > a.d_s[z], \tag{28}$$

where $d_s[z] = s^*[\check{z}] - s^*[z] = 1 - s^*[z]$.

The probability of an error occurring due to $w[z] > a.d_s[k]$ is

$$p(w[z] > a.d_s[z]) = 1 - P_w(a.d_s[z]) \tag{29}$$

where P_w is the Cumulative Distribution Function (CDF) of p_w.

Then, the PDF of $\hat{z} - z^*$, i.e. the PDF of a given position of the residue $\mathbf{r}$, can be defined as

$$p_r[z] \propto 1 - P_w(a.d_s[z]) \tag{30}$$

To determine the distribution of the random variable W, first lets define it as $w = x+(-y)$. The random variables x and y are independent and identically distributed (i.i.d.) from a Rayleigh Distribution.

$$p_x = \frac{x}{\sigma^2} e^{-\frac{x^2}{2\sigma^2}}, \text{ for } x \geq 0 \tag{31}$$

and

$$p_{-y} = \frac{-y}{\sigma^2} e^{-\frac{y^2}{2\sigma^2}}, \text{ for } y \leq 0, \tag{32}$$

in which σ denotes the scale parameter of the Rayleigh Distribution.

The CDF of the difference between two random variables is defined as

$$P_w(w) = \iint_{-\infty}^{\infty} P_x(x)\, p_{-y}(y)\, dx\, dy. \tag{33}$$

Changing the variable $-y$ for $w - x$ and substituting in Eq. 33 leads to

$$P_w(w) = \int_{-\infty}^{\infty} P_x(w + y)\, p_y(w - x)\, dy, \text{ for } w < 0, \tag{34}$$

which is equivalent to

$$P_w(w) = \int_0^{\infty} P_x(x)\, p_y(x - w)\, dy, \text{ for } w < 0. \tag{35}$$

As x and y are i.i.d., the distribution of $w = x - y$ and $-w = y - x$ must be equal, making the distribution of w symmetric around 0. This results in

$$P_w(w) = \frac{w\sqrt{\pi} e^{-\frac{w^2}{2\sigma^2}}}{4\sigma}.\text{erfc}\left(\frac{w}{2\sigma}\right) - \frac{e^{-\frac{w^2}{2\sigma}}}{2} + 1, w \geq 0, \tag{36}$$

where $\text{erfc}(\cdot)$ denotes the complimentary error function. This expression can be approximated by the CDF of a normal distribution $\mathcal{N}(0, (4 - \pi)\sigma^2)$, so that

$$P_w(w) = \frac{1}{2}\left[1 + \text{erf}\left(\frac{|w|}{\sigma\sqrt{2(4 - \pi)}}\right)\right]. \tag{37}$$

Considering the approximation and applying it into Eq. 30, the following is obtained

$$p_r[z] \propto \frac{1}{2}\left[1 - \text{erf}\left(\frac{|a.d_s[z]|}{\sigma\sqrt{2(4 - \pi)}}\right)\right]. \tag{38}$$

Since P_w is symmetric around 0, so is $p_r[z]$. This is in agreement with the idea in Chapter 4 that the maximum amplitude of a column, a, is tied to the variance of the residue.